Characterization of proven Late Cretaceous Reservoir rocks in the Gulf of Gabes: Integrated case study

Senda Boughalmi, Yves Géraud, Danièle Grosheny, Sonia Ben Alaya, Mohamed Hedi Negra

BSGF - Earth Sciences Bulletin 2023, 194, 8
© S. Boughalmi *et al.*, Published by EDP Sciences 2023
https://doi.org/10.1051/bsgf/2022020

BSGF
Earth Sciences Bulletin
Available online at:
www.bsgf.fr

Open Access

Characterization of proven Late Cretaceous Reservoir rocks in the Gulf of Gabes: Integrated case study

Senda Boughalmi[1,*], Yves Géraud[2], Danièle Grosheny[2], Sonia Ben Alaya[3] and Mohamed Hedi Negra[1]

[1] Faculty of Sciences of Tunis, Tunis El Manar University, U.R. Pétrologie Sédimentaire et Cristalline, Campus Universitaire, Tunis 2092, Tunisia
[2] Université de Lorraine, CNRS, GeoRessources, F-54000 Nancy, France
[3] Entreprise Tunisienne d'Activités Pétrolières (ETAP), Charguia II, Tunis 2053, Tunisia

Received: 15 May 2021 / Accepted: 8 December 2022 / Publishing online: 24 May 2023

Abstract – Microstructural features control the petrophysical properties of rocks. Of these, pore size is particularly sensitive when non-wetting fluids saturate the reservoir. The pore networks and physical properties (helium, water and mercury saturation porosity, bulk density, nitrogen permeability, P-wave velocity and thermal conductivity) of different rock types from a productive Upper Cretaceous (Coniacian) reservoir in the tunisian offshore are measured on hydrocarbon-washed samples. The facies sampled of Douleb Member are wackestone, packstone and grainstone textures as well as dolostone, dolomitized packstone and anhydrite textures. Based mainly on the results obtained by mercury injection, the porous facies of the Coniacian Douleb Member are characterized by a complex pore system with a large morphological and pore size variability in the rock. Porosity values range from 0.3 to 23.6%, bulk densities vary from 2.05 to 2.92 g.cm^{-3}. The permeability is variable from 3760 mD to values below 0.01 mD (measurement limit of the device). P-wave propagation velocity values range from 2060 to 6084 m.s^{-1} and thermal conductivity varies from 1.43 to 3.77 W.m^{-1}.K^{-1}. The oil-impregnated facies with the best petrophysical characteristics are mainly the rudist-rich limestones and dolomites of the first unit (U1) of the Douleb Member. The well-sorted grainstones with small rudist debris and peloids have the best reservoir qualities. Porosity is the first order characteristic that controls petrophysical properties. The variability of permeability values around this first-order relationship is attributed to variations in the size of the pore access thresholds and connectivity. The variability in velocities is due to the shape of the voids, while the variability in thermal conductivity measurements is due to the nature of the contacts between the grains.

Keywords: Late Cretaceous / Douleb Member / Tunisia / carbonate reservoir / petrophysics / diagenesis

Résumé – Caractérisation d'un réservoir prouvé du Crétacé Supérieur dans le Golfe de Gabès. Les caractéristiques microstructurales contrôlent les propriétés pétrophysiques des roches. Parmi celles-ci, la taille des pores est particulièrement sensible lorsque des fluides non-mouillants saturent le réservoir. Les réseaux poreux et les propriétés physiques (porosité par saturation à l'hélium, à l'eau et par injection de mercure, densité apparente, perméabilité à l'azote, vitesse de propagation des ondes P et la conductivité thermique) sont mesurés sur des échantillons lavés des hydrocarbures prélevés à partir d'un réservoir productif d'âge crétacé supérieur (Coniacien) situé dans l'offshore tunisien. Les facies échantillonnés du Membre Douleb sont de texture wackestone, packstone et grainstone, de texture dolostone et packstone dolomitisé ou encore composés d'anhydrite. En se basant essentiellement sur les résultats obtenus par injection de mercure, les faciès poreux du membre Douleb se caractérisent un système poreux complexe présentant une grande variabilité morphologique et de la taille des pores. Les valeurs de porosité sont comprises entre 0,3 et 23,6 %, les densités apparentes varient de 2,05 à 2,92 g.cm^{-3}. La perméabilité varie de 3760 mD à des valeurs inférieures à 0,01 mD (limite de mesure de l'appareil). Les valeurs de vitesse de propagation des ondes P sont comprises entre 2060 et 6084 m.s^{-1}, et celles de conductivité thermique varient entre 1,43 et 3,77 W.m^{-1}.K^{-1}. Les facies imprégnés d'huile qui présentent les meilleures

*Corresponding author: sendaboughalmi@gmail.com

caractéristiques pétrophysiques sont essentiellement les calcaires riches en débris de rudistes et les dolomies de la première unité (U1) du membre Douleb. Les grainstones bien classés à petits débris de rudistes et pelletoïdes présentent les meilleures qualités réservoirs. La porosité est, au premier ordre, la caractéristique qui contrôle les propriétés pétrophysiques. La variabilité des valeurs de perméabilité autour de cette relation de premier ordre est attribuée à des variations de la taille des seuils d'accès aux pores et de la connectivité. Celle des vitesses est due à la forme des vides, alors que celle observée pour les mesures de conductivité thermique dépend de la nature des contacts entre les grains.

Mots clés : Crétacé supérieur / membre Douleb / Tunisie / réservoir carbonaté / pétrophysique / diagenèse

1 Introduction

Carbonate formations are largely prospected for petroleum, water or geothermal resources. The porous network characteristics of the reservoirs (pore volume, pore size, pore shape and connectivity) largely contribute to the reservoir properties: permeability, thermal conductivity and elastic properties (Belikov, 1967; Zinszner and Pellerin, 2007; Nabawy, 2015; Haffen *et al.*, 2017). These porous network characteristics, porosity and transfer properties, permeability and thermal conductivity, are due to a large variety of sedimentary, structural or diagenetic processes (Lucia, 1999; Ali *et al.*, 2010; Verwer *et al.*, 2011; Ghafoori *et al.*, 2018). A large data set is already published on petrophysical properties of carbonate reservoirs (Ehnenberg *et al.*, 2006; Al-Tooqi *et al.*, 2014; Nabawy and Kassab, 2014; El Husseiny and Vanorio, 2016; Salah *et al.*, 2016; Njahi *et al.*, 2017), but a low amount of data is available on strictly reservoirs in place except through the analysis of surface analogues which are not saturated with hydrocarbon.

The Late Cretaceous carbonate series are well represented on the southern margin of the Tethys and they are the subject of numerous stratigraphic, sedimentological and tectonic studies (Masse and Philip, 1981; Philip, 1985; Skelton and Gili, 1991; Grasso *et al.*, 1999; Abdallah *et al.*, 2000; Scott, 2003; Philip, 2003; Skelton, 2003; Grosheny *et al.*, 2013; Lebedel *et al.*, 2015; Jaballah, 2017; Bachari *et al.*, 2019). However, the petrophysical rock properties are poorly documented. Development of these series is maximal during Turonian and Coniacian and their demise occurs at the Coniacian-Santonian limit (Camoin, 1989; Grosheny *et al.*, 2013).

In Central and Southern Tunisia, these series are generally rich in rudists (Zagrarni *et al.*, 2003; Touir *et al.*, 2009; Boughalmi *et al.*, 2019; Boughalmi, 2020; Negra and Jaballah, 2021). They are characterized by variations in thickness and facies (Salmouna-Jomaa *et al.*, 2014; Jaballah, 2017). These variations appear to be controlled by local (tectonic) and global (eustatic) factors.

From the petroleum system point of view, the Late Cretaceous carbonate facies in Tunisia, especially those of the Cenomanian-Turonian (Gattar and Bireno Members) and those of the Coniacian (Douleb Member) belonging to the Turonian-Early Campanian Aleg Formation, are known for their good reservoir quality. In fact, they are productive in several sectors of Tunisia, notably in the region of Sfax and the Gulf of Gabes (Burollet, 1956; M'Rabet *et al.*, 1995; Lansari *et al.*, 2010) and more specifically in several oil fields especially those of Guebiba, Gremda, El Ain, Rhemoura and Miskar (M'Rabet *et al.*, 1995; Chaabouni, 1996; Saïdi *et al.*, 1997; Troudi *et al.*, 1999; Zagrarni *et al.*, 2003; Lansari *et al.*, 2010). Studies have shown that the proven reservoirs in the study area are characterized by facies variations (Jaballah, 2017; Salmouna-Jomaa, 2017; Boughalmi, 2020). These variations can directly affect the reservoir potential of these series and their impregnation by hydrocarbons. In addition, several diagenetic factors either may improve or reduce their reservoir quality (Nabawy and Kassab, 2014).

The objective of this paper is to define the petrophysical characteristics and especially reservoir properties of carbonate oil-bearing core samples within a Coniacian rudist reservoir (Douleb Member, Fig. 1). To better understand the relationship between the various petrophysical properties of rocks, a large set of data is acquired, especially to define relationships between transfer properties and microfacies characteristics. Connected porosity and permeability define the reservoir properties and quality. P-waves velocity is a key parameter to inverse seismic data and convert time to depth while thermal conductivity is a key to model diagenetic processes and organic matter maturation.

Reservoir quality mostly depends on the characteristics of the pore network, pore volume, pore size, pore shape and pore connectivity while P-wave velocity and thermal conductivity are controlled by the previous porosity parameters and by several parameters concerning the solid phases, such as mineral composition, grain size, grain shape and type of grain contacts (Belikov, 1967; Bourbié *et al.*, 1986; Denis, 1990; Guéguen and Palciauskas, 1992; Wang and Nur, 1992; Popov *et al.*, 1999; Homand and Duffaut, 2000; Popov *et al.*, 2003; Hartmann *et al.*, 2005; Zinszner and Pellerin, 2007; Nabawy, 2015; Nabawy and Géraud, 2016; Haffen *et al.*, 2017).

Finally, it is proposed arguments to explain why oil impregnation does not concern the whole carbonate reservoir and is defined which facies have the best petrophysical characteristics of the productive well.

2 Geological setting

The studied well is in the Northeast of the Gulf of Gabes approximately 110 km towards the east-southeast from Sfax (Fig. 2). This well is in the eastern part of the Tunisian Sahel in the open sea. It lies on the Pelagian Platform, where during Early Cretaceous to Eocene an incipient rift system developed. This rift system is composed of a series of horsts and tilted blocks (Martinez and Truillet, 1987; Zouari *et al.*, 1999).

The Gulf of Gabes is a subsident domain of the Pelagian Platform and marks the sinking of the Saharan Platform towards the central Mediterranean (Ben Ayed, 1986). In this oriental area, under a thick Neogene series, subsurface data

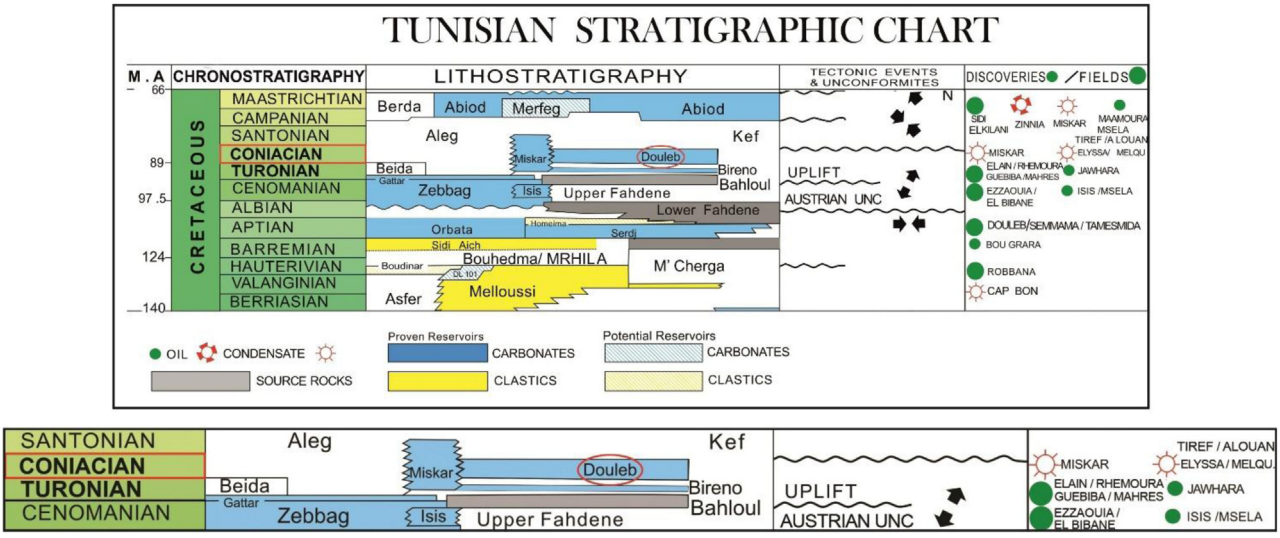

Fig. 1. Tunisian stratigraphic chart (ETAP).

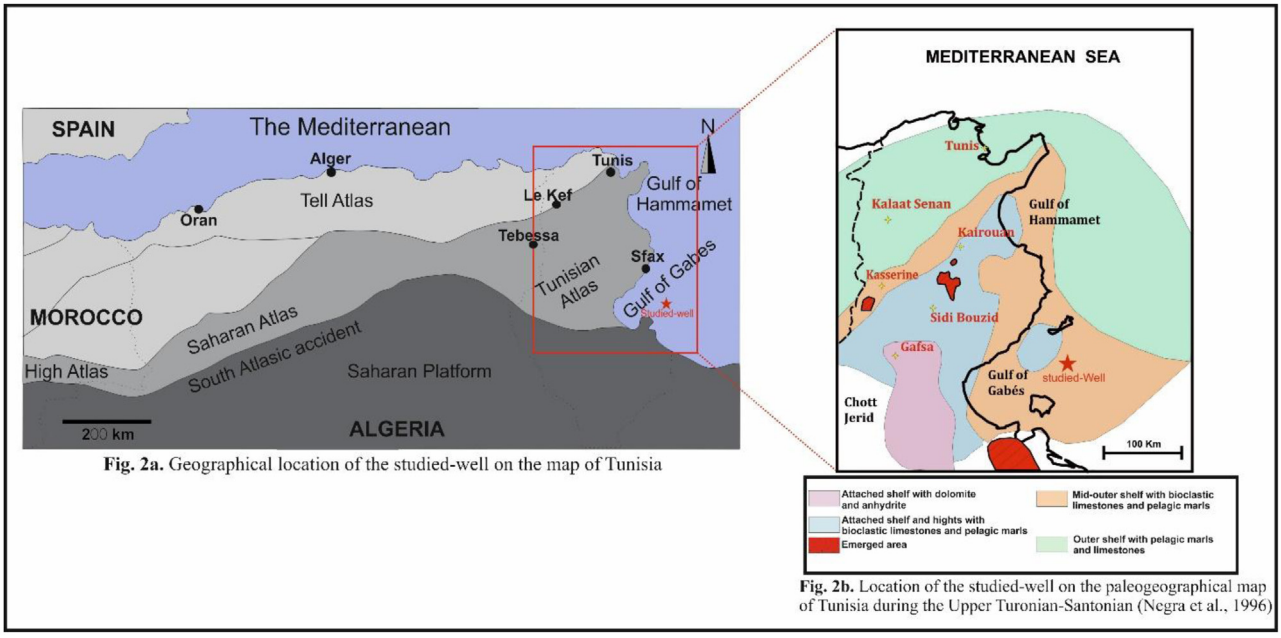

Fig. 2a. Geographical location of the studied-well on the map of Tunisia

Fig. 2b. Location of the studied-well on the paleogeographical map of Tunisia during the Upper Turonian-Santonian (Negra et al., 1996)

Fig. 2. Position of the studied-well on the map of Tunisia.

reveal slightly undulating in NE-SW directions (Ben Ayed, 1986; Martinez and Truillet, 1987; Touati and Rodgers, 1998).

The studied carbonate reservoir corresponds to the Coniacian rudist interval comprising the Late Cretaceous (Fig. 3), Paleogene and Neogene series. It is sealed by the clays of the El Haria Formation. The Cenomanian-Turonian Bahloul Formation, covering the east-central part of Tunisia, is considered as a main source rock for the Cretaceous reservoirs, notably the Douleb one.

Concerning the paleogeographic setting of the Late Cretaceous, the Cenomanian-Turonian transition is marked by laminated limestones with marly intercalations of the Bahloul Formation deposited in a relatively deeper environment (Burollet, 1956; Hanini *et al.*, 2004; Caron *et al.*, 2006; Robaszynski *et al.*, 2007; Zagrarni *et al.*, 2008). The Turonian-Early Campanian Aleg Formation is composed of limestones from deep marine environment that show many variations of thickness due to subsidence (Salaj, 1978). The carbonate Bireno and Douleb Members are the lateral equivalents of some marly intervals of the Aleg Formation towards the Central Tunisia (Lansari *et al.*, 2010; Jaballah and Negra, 2016). During the Campanian-Maastrichtian period, the

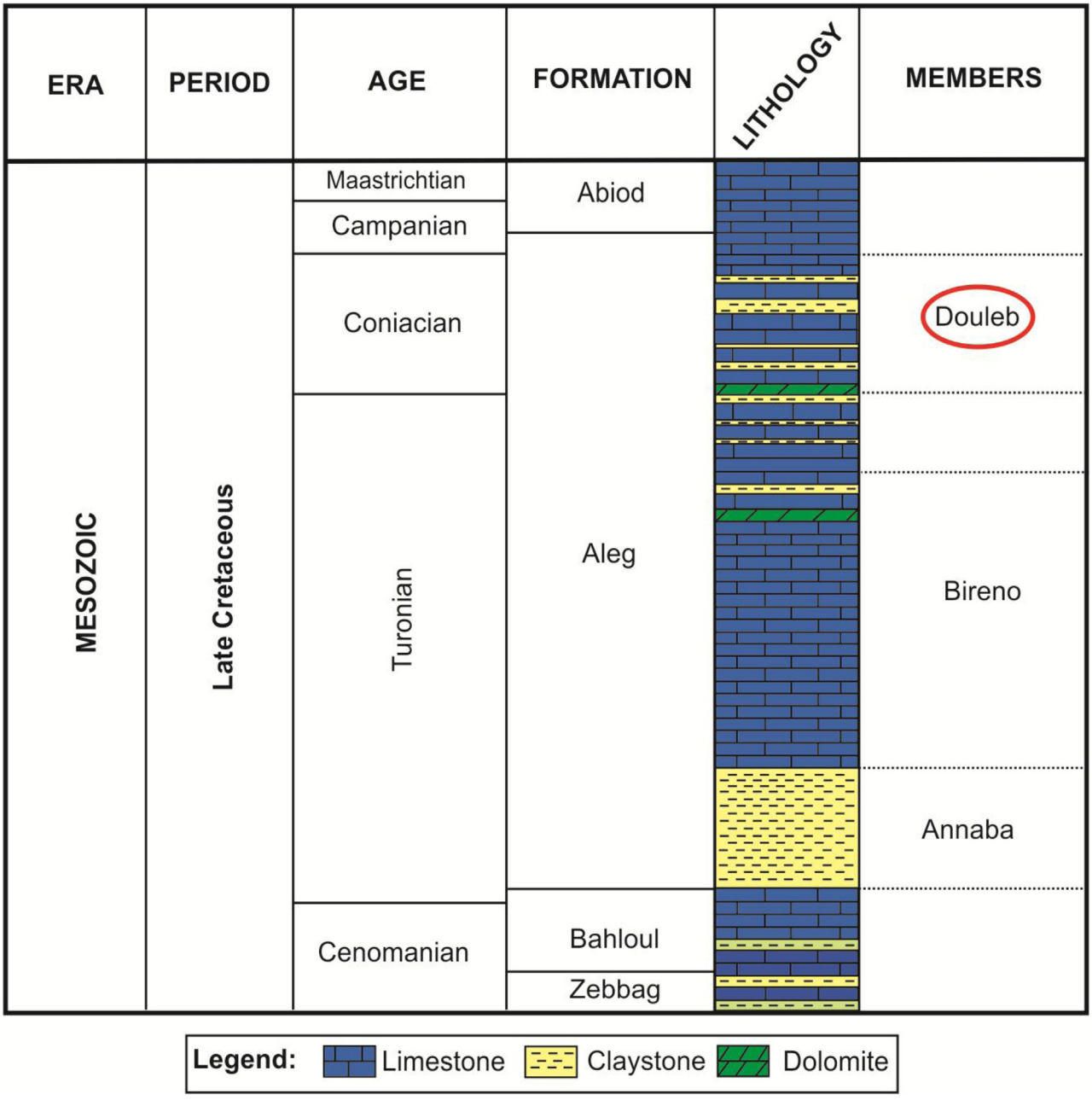

Fig. 3. Lithostratigraphic column of the different Cretaceous formations intersected in the studied-well.

micritic chalky limestones and the marls of the Abiod Formation were deposited, covering the marls of the Aleg Formation. This unit is mainly composed of limestones settled in open marine sea with variations in sea level (Burollet, 1956; Khessibi, 1978; Melki and Negra, 2004; Negra and Gili, 2004; Bey *et al.*, 2012).

Facies of the Douleb Member are the object of this study (Fig. 2b); they form a large carbonate platform above a low subsidence floor. The shallow marine sedimentation is bioclastic, oolitic, gravelly and locally rudist-rich lithosomes. This platform can be subdivided into an internal platform, a median to external platform and an emerged zone (Zagrarni, 1996; Saïdi *et al.*, 1997).

3 Materials and methods

The characterization of the reservoir is obtained by qualitative or semi-quantitative petrographical and sedimentological analyses, and by quantitative petrophysical measurements. The adopted methodology is schematized on the chart of Figure 1S (see Supplementary Material).

Table 1. Microfacies description of the Coniacian interval of the studied-well.

Microfacies	Description
Mf1	Dolomitized packstone: rich in rudists
Mf2	Grainstone: fine-grained, well sorted with small rudists, peloids and some benthic foraminifera
Mf3	Packstone-grainstone: small rudist-debris, echinoderms and some peloids
Mf4	Packstone: calcispheres, planktonic foraminifera and some debris
Mf5	Packstone: miliolids, ostracods, planktonic foraminifera and peloids
Mf6	Packstone: large rudist debris, peloids and some intraclasts
Mf7	Wackestone: fragmented rudists
Mf8	Packstone: oolites, micritized bioclasts, echinoderms, gastropods and benthic foraminifera
Mf9	Dolostone
Mf10	Anhydrite facies
Mf11	Packstone: peloids, some benthic foraminifera and echinoderm-debris
Mf12	Sandy wackestone: calcispheres, rare planktonic foraminifera and some intraclasts

3.1 Sedimentological study

For sedimentological study, first, macroscopic analysis was done to recognize the main sedimentological features of ten cores totaling 112 m in length, secondly, the microscopic analyses of 176 thin sections were conducted, using optical microscopy (highlighting the texture, structure, bioclasts contents, porosity type and the diagenetic process characterizing the studied interval). The microscopic analysis was also done using the Scanning Electron Microscopy (SEM), on 19 samples. Sedimentological analysis led to the classification of 12 different microfacies noted (Mf1 to Mf12) and summarized in Table 1.

3.2 Petrophysical study

Prior to the petrophysical measurements, samples were washed thoroughly to extract the oil and mineral salts existing in their porosity. Xylene or toluene is used to extract oils and methanol is used to remove mineral salts using an electrical Soxhlet extractor. After that, they were dried properly without any effect on the clay minerals in an oven at a temperature of 60° C till they have reached a constant weight.

Measurements of porosity, permeability, P-waves velocity and thermal conductivity are carried out on 26 samples, 2.54 cm (1 inch) in diameter and between 3.4 and 4.1 cm in length. They belong to the Coniacian interval of the well drilled in the Gulf of Gabes. Except for permeability measurements made in the ETAP laboratory (Tunisia), all the measurements are made at the GeoRessources Laboratory (Nancy).

3.2.1 Porosity measurements

The porosity is defined as the ratio of void volume to total volume of a material (Zinszner and Pellerin, 2007). In the rock, porosity could be composed by connected or isolated pores with various shapes (Norton and Knapp, 1977).

Helium, water and mercury are fluids used to saturate the samples and to determine the pore volume. The mercury injection porosimetry gives the distribution of the porous volume *versus* the threshold. The porosity classification proposed by Al-Marzouqi *et al.* (2010) is used. Microporosity has pore size lower than 0.5 μm, the pore size of the mesoporosity ranges from 0.5 and 5 μm, while microporosity has pore size higher than 5 μm.

3.2.1.1 Porosity by water saturation

The triple weight method, or Archimeds method, uses a wetting fluid (water) to saturate the porosity (Dullien, 1979) and follows the procedure of the standard RILEM (Rilem, 1978). Samples were placed in a vacuum chamber for 24 h, beside distilled water was degassed and then used to fill samples' chamber following the progression of the sample capillarity fringe. Once, samples were completely submerged, they stayed at least 24 h until they reached a constant weight. The connected porosity is given by:

$$\varphi = \frac{w_1 - w_d}{w_1 - w_2} \times 100, \tag{1}$$

With φ is the porosity (%), W_1 is the weight of sample saturated under vacuum with water (g), W_2 is the weight of saturated sample under hydrostatic condition (immersed under water; g) and W_d is the dry weight of the sample (g).

The bulk density (d_b) is calculated as follows:

$$d_b = \frac{w_d}{w_1 - w_2}, \tag{2}$$

With d_b is the bulk density ($g.cm^{-3}$).

3.2.1.2 Porosity by helium saturation

The "UltraPoreTM300" helium porosimeter uses the "Boyle" law to determine the grain volume from the expansion of a known mass of helium into calibrated sample holder. Helium, being a rare and light gas, has the property of easily penetrating and saturating the pores of the sample.

Boyle's law is expressed as follows:

$$\frac{P_1 V_1}{T_1} = \frac{P_2 V_2}{T_2}, \tag{3}$$

With P_1 is the initial pressure (atm), V_1 is the initial volume (cm^3), T_1 is the initial absolute temperature (°C), P_2 is the expanded pressure (atm), V_2 is the expanded volume (cm^3) and T_2 is the expanded absolute temperature (°C).

The equation used to calculate grain volume is derived from the basic Boyle's law equation as follows:

$$P_1 V_{holder} = P_2 \left(V_{holder} - V_{grain}\right), \tag{4}$$

$$V_{grain} = V_{holder} - (P_1/P_2 \times V_{holder}), \tag{5}$$

With V_{holder} is the holder's volume (cm^3) and V_{grain} is the volume of solid phase (cm^3). Knowing the mass of the sample under dry condition, the grain density (d_{sp}), $g.cm^{-3}$, is calculated as follows (Zinszner and Pellerin, 2007):

$$d_{sp} = \frac{w_d}{V_{grain}}. \tag{6}$$

The porosity is calculated using the solid phase density obtained from helium pycnometer test and the bulk density obtained from triple weight measurements with the following equations (Zinszner and Pellerin, 2007):

$$\varphi = 1 - \left(\frac{d_b}{d_{sp}}\right) \times 100. \tag{7}$$

3.2.1.3 *Porosity by mercury injection*

The use of mercury (non-wetting phase) as a saturating liquid provides access to a more complete data set with the distribution of invaded pore volumes *vs.* their threshold sizes, the percolation threshold, and the trapped and the free porosities (Washburn, 1921; Wardlaw and Taylor, 1976; Wardlaw and Cassan, 1978; Kloubek, 1981; Wardlaw and McKellar, 1981; Li and Wardlaw, 1986).

Mercury is a non-wetting liquid and a pressure must be applied to enter the voids of the sample. Injection pressure depends on the radius of the capillaries; it is defined by Young–Laplace's law:

$$P = \frac{4\sigma\cos\theta}{d}, \tag{8}$$

With P (Pa) is the pressure, d (μm) is the length distance of two opposite walls of a pore expressed by an effective radius, σ is the surface tension of mercury (485 $dynes.cm^{-1}$) and θ is the contact angle (130°).

Micrometrics Autopore IV series 9200 porosimeter allows pressures range from 0.004 to 220 MPa, *i.e.* the pore access sizes range between 307 μm and 0.005 μm.

Testing process is decomposed in three main sequences. The first is a drainage sequence, composed of two phases, a low pressure injection phase from 0.004 to 0.2 MPa, and a high pressure injection phase from 0.1 to 220 MPa. The second is an imbibition sequence from 220 to 0.1 MPa. The third is a drainage sequence again, from 0.1 to 220 MPa. The duration of the test is four hours.

Several porosity volumes and threshold values are determined. The connected porosity is saturated during the first drainage sequence, it is the mercury's volume injected at 220 MPa. It is divided into low and high pressures porosity parts, measured between 0.004 and 0.1 MPa and 0.1 and 220 MPa, respectively. The trapped and the free porosities, TrP and FP, respectively, are obtained using the two last sequences. Due to the measurement conditions, these two porosity parameters must be interpreted using only the high-pressure porosity part, CP, obtained during the first drainage sequence. These values are characteristic of the porosity volume connected through thresholds between 7 and 0.004 μm. Trapping is mainly controlled by the ratio between the pore size and pore throat. If this ration is higher than 6, mercury is trapped in ink-bottle shape pores (Wardlaw and Yu, 1988).

From the cumulative injection curve, three threshold values are determined using the first drainage curve. First, the percolation threshold defined as the inflexion point of the curve, it is built graphically from the curve. Two other diameters values are defined at the beginning and the end of the injection sequences, d1 and d2, and these elements define the spreading of threshold values (ST). "d1" is defined as the last point of the low deep section at the beginning of the injection curve and "d2" is the first point of the plateau in the final part of the injection curve. The last element, defined to describe the porosity distribution, is the incremental intrusion curve decomposed in several porosity families.

3.2.2 Permeability

Permeability (K) refers to the ability of a material to transfer fluids, and therefore it is closely related to the intrinsic properties of the porous network, mainly the size, the shape, and the connectivity (Scheidegger, 1974; Homand and Duffaut, 2000).

The gas permeameter "UltraPermTM 400" uses Darcy's law to calculate the permeability from the gas flow rate and the measured upstream and downstream pressures.

Measurements are performed using Nitrogen under low confining pressure (2 MPa). As permeability measurements did not exhibit slip-flow phenomena between gas molecules and solid walls, Klinkenberg effect was not considered (Klinkenberg, 1941).

Darcy's Law:

$$Q = KA\frac{\Delta P}{L\mu}, \tag{9}$$

With Q is the volumetric flow rate ($m^3.s^{-1}$), K is the permeability coefficient (mD), A is the area of the sample section perpendicular to the flow (cm^3), ΔP is the pressure difference between the top and the bottom of the sample (atm), L is the length of the sample (cm) and μ is the viscosity of fluid (cP).

3.2.3 P-wave velocity

The measurement of the velocity of compressed or primary longitudinal P-waves representing the vibration of the particles parallel to the direction of propagation of the wave (Zinszner and Pellerin, 2007; Boulanouar *et al.*, 2013). The propagation

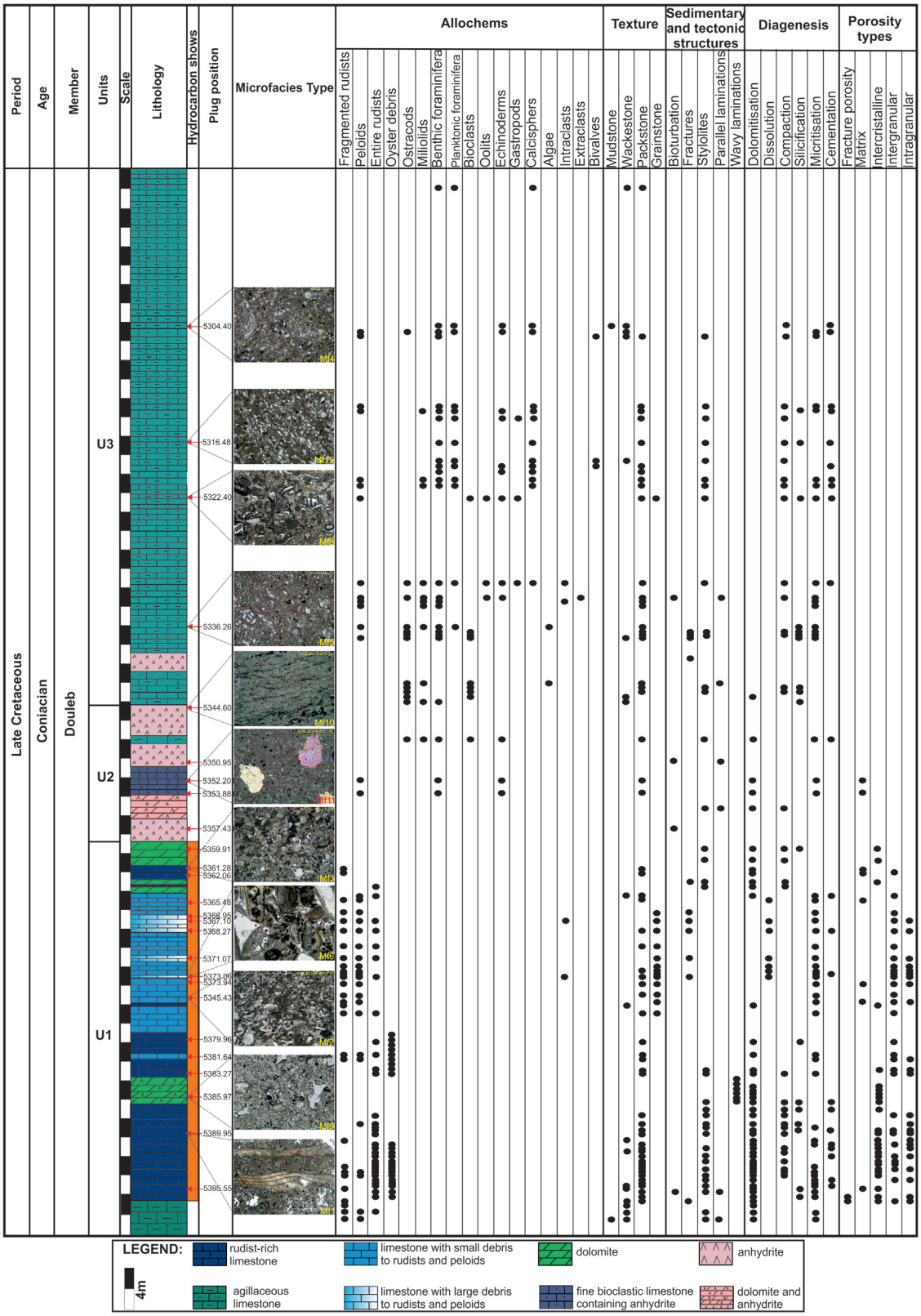

Fig. 4. A detailed log showing the Douleb Member in the study area.

velocity depends on the mineralogical content, the grain shape and contact, the porosity, and the pore space geometry, particularly the cracks distribution (Homand and Duffaut, 2000). This measure makes it possible to evaluate elastic physical properties of rocks, like Young's modulus or Poisson's ratio (Bourbié *et al.*, 1986; Wang and Nur, 1992).

The measuring equipment is composed by two piezoelectric transducers of frequency 54 Hz and a Pundit Lab pulse generator. After determining the path's length (L) and the propagation time of the ultrasonic waves (t), the propagation velocity of P-waves is given by the formula:

$$V(m/s) = \frac{L(m)}{t(s)}. \quad (10)$$

3.2.4 Thermal conductivity

Thermal Conductivity Scanning (TCS) technique is based on the variation of temperature at a sample surface following a known and controlled heat input (Popov *et al.*, 1983, 1985, 1999). The experimental device is composed by a movable block composed of two temperature sensors sensitive to electromagnetic radiation and a source of heat located between both captors so that it is possible to measure the temperature of the sample before and after heating.

To obtain an absolute value of the thermal conductivity of the analysed material, two known thermal conductivity standards (λstd) are placed on each side of the sample. The thermal conductivity of the material will be determined from λstd and the ratio of temperature differences:

$$\lambda(x) = \lambda std \frac{\theta std}{\theta(x)}. \quad (11)$$

Quartz standards are used for dry samples.

4 Results and discussion

4.1 Lithostratigraphy

In the studied well, thickness of Douleb Member is 112 m. According to the lithology and the fossiliferous content, three distinct lithological units are highlighted (Fig. 4):

– Unit 1 (U1): Carbonate unit with a thickness of 41.50 m, mainly formed of rudist-rich limestones intercalated by two dolomitic layers showing laminations and wavy structures (Figs. 5A and 6A). The base of this unit is formed of clayey limestones (Fig. 5B) showing a wackestone-packstone texture with rudist-debris, surmounted by limestones with wackestone-packstone texture containing large debris of entire and joined rudists (Figs. 5C and 5D) of Hyppuritidae and Radiolitidae type (Negra and Philip, 1986; Fig. 6B), then by porous limestones showing fining upward sequences (Figs. 5E–5G) of packstone-grainstone texture essentially formed of peloids and partly micritized rudists. The latter show bioclasts of various sizes: well sorted to small debris (Figs. 6C and 6D) and badly sorted facies containing debris of different sizes but frequently coarse (Figs. 6E). The coarse facies are marked by the presence of some fractures open to partly clogged, horizontal to gently dipping.

– Unit 2 (U2): This unit, with a thickness of 19.80 m, is essentially formed of anhydrite (Figs. 5H and 7A) of beige colour and bioturbed. This anhydrite unit is intercalated by centimetric layers of argillaceous limestones, laminated and bioturbed corresponding to:

- Packstones with peloids, echinoderm-debris and some benthic foraminifera, containing large crystals of anhydrite (Fig. 6F);
- Wackestones-packstones containing rudist-debris, echinoderm-debris, miliolids, benthic foraminifera and ostracod-debris;
- Wackestones-packstones rich in ostracods (entire and in debris).

– Unit 3 (U3): This unit (50.70 m thick) is formed of fine micritic carbonates, partly argillaceous, nodular, and laminated (Fig. 5I). This unit consists of an alternation of varied facies such as:

- Wackestones-packstones with calcispheres, planktonic foraminifera, some debris and intraclasts (Figs. 7B and 7C);
- Packstones with miliolids, ostracods, benthonic foraminifera and some debris (Fig. 7D);
- Packstones with oolites, peloids, echinoderms, gastropods and benthonic foraminifera (Figs. 7E and 7F);
- Packstones with peloids, some benthonic foraminifera and echinoderm debris.

This unit which is marked by the abundance of stylolites (Figs. 5I, 7B and 7D) and cemented fractures, is mainly formed of micrite showing automorph quartz crystals (Fig. 7C), framboidal pyrite, phosphate (Fig. 7B) and glauconite.

4.2 Petrophysical properties

The results of measurements of density, porosity, permeability, P-waves velocity, and thermal conductivity are presented in Table 1S (see Supplementary Material).

4.2.1 Porosity

4.2.1.1 Connected porosity values

The obtained values with the three methods (water, helium, and mercury saturations) are homogeneous and almost consistent with high regression coefficients ($R^2 = 0.99$) showing the certainty of the porosity values with different measurement methods despite of different size of samples used in the different methods (Fig. 8a). Three rock-types of samples are distinguishable based mainly on water and helium porosimetry data (Fig. 8b). The first one (Rt1) consists of samples that have porosity lower than 3%. In the second group (Rt2), porosity ranges from 14 to 19%; for the third one (Rt3), porosity values range from 21 to 24%.

If water porosity and helium porosity values show a good correlation (Fig. 8b); however, porosity values obtained by Hg-injection tests are quite dispersed compared to helium porosity values (Fig. 8c). In fact, this probably illustrates the sample size effect. Indeed, samples used for Hg-injection test are much

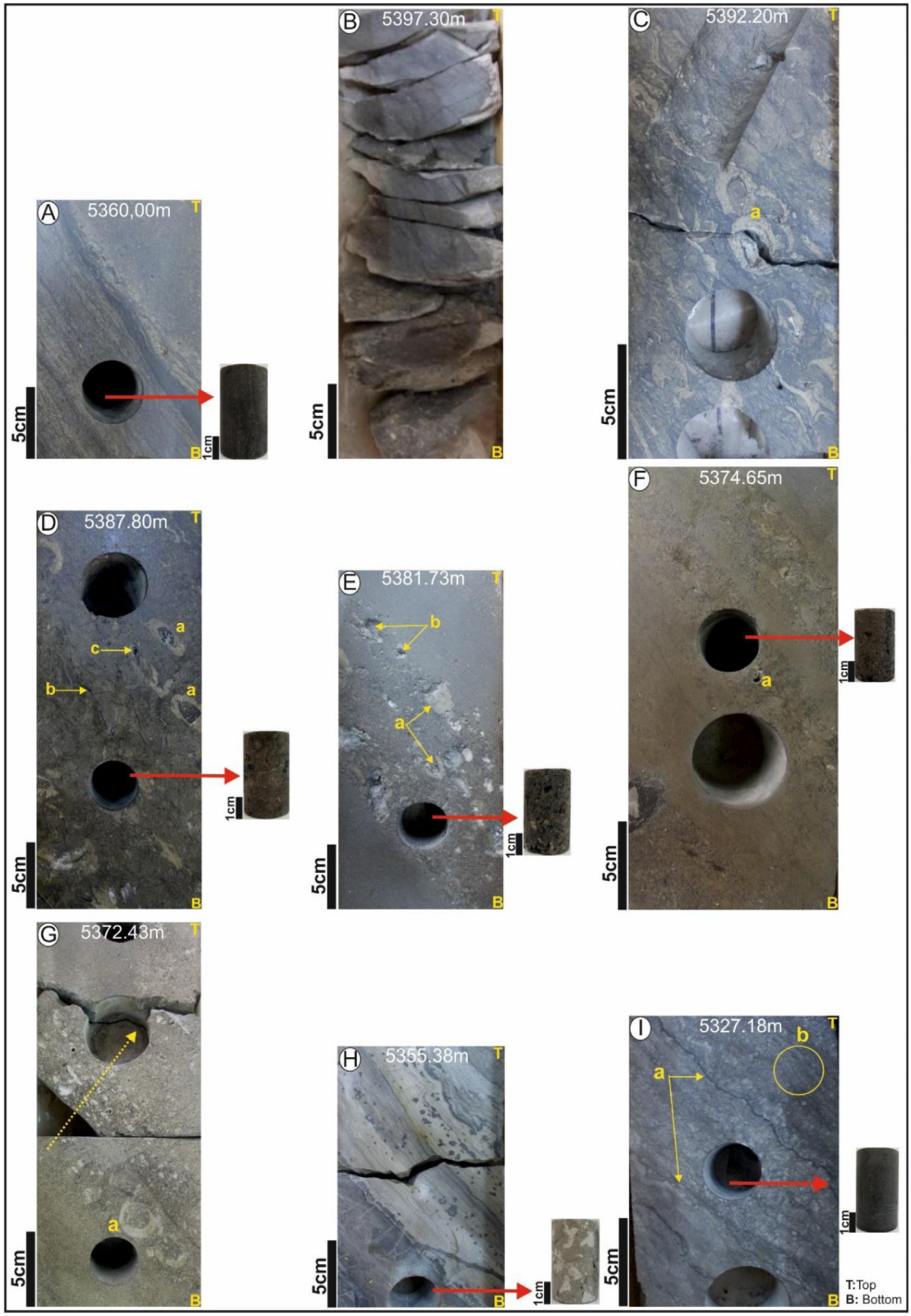

Fig. 5. The main macrofacies of the Douleb Member. A: Brown dolomite, oil-impregnated and laminated. B: Clayey limestone. C: Brown limestone, oil-impregnated with whole and rudist shells touching each other (a). D: Brown colored limestone rich in rudists (a) and oysters-debris (b) showing macropores (c). E: Oil-impregnated brown bioclastic limestone, rich in rudist debris (a) and showing an important macroporosity (b). F: Oil-impregnated brown limestone, fine bioclastic limestone showing a fining upward sequence and a macroporosity (a). G: Limestone beige-brown, bioclastic rich in rudists (a) showing a granular-decreasing sequence (yellow arrow). H: Brown anhydrite facies with parallel laminations. I: Gray limestone, very fine bioclastic, showing compaction stylolites (a) very serrated and laminated structures (b).

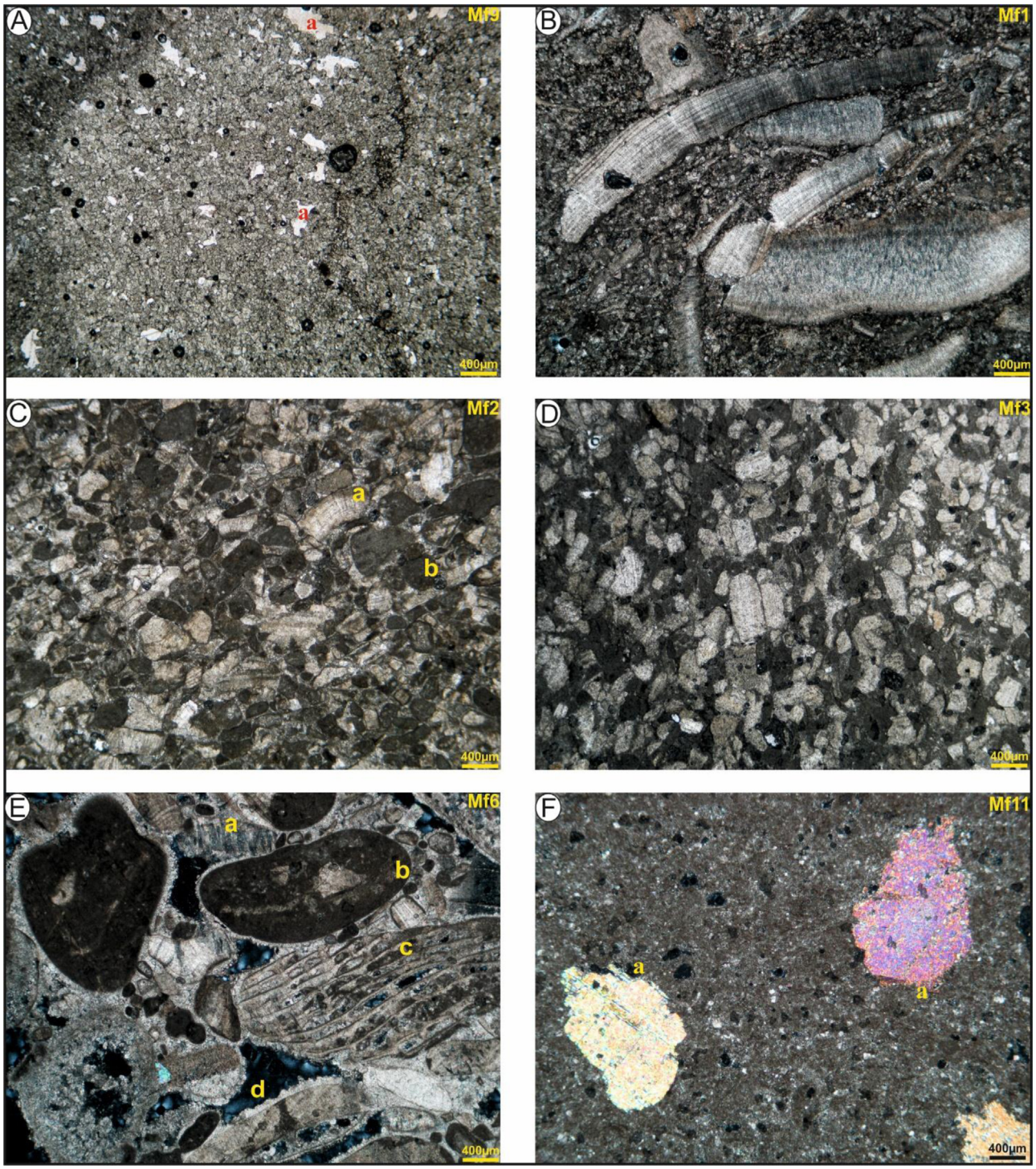

Fig. 6. The bioclastic and porous facies of the Douleb Member (Units U1 and U2). A: (Mf9) Dolomitic microfacies showing an intercrystalline porosity (a). B: (Mf1) Dolomitized packstone rich in rudist shells of Hippuritidae type. C: (Mf2) Grainstone with small debris of rudists (a) and peloids (b); small and well sorted debris. D: (Mf3) Packstone-grainstone with small well sorted debris of rudist shells of Hippuritidae type and peloids. E: (Mf6) Packstone with large peloids (b) and large debris of rudists shells of (a) Hippuritidae and (c) Radiolitidae types, (d) development of calcitic cement around allochems: rudist and peloids. F: (Mf11) Fine packstone with small peloids, rare benthic foraminifera and echinoderms, containing large crystals of anhydrite (a).

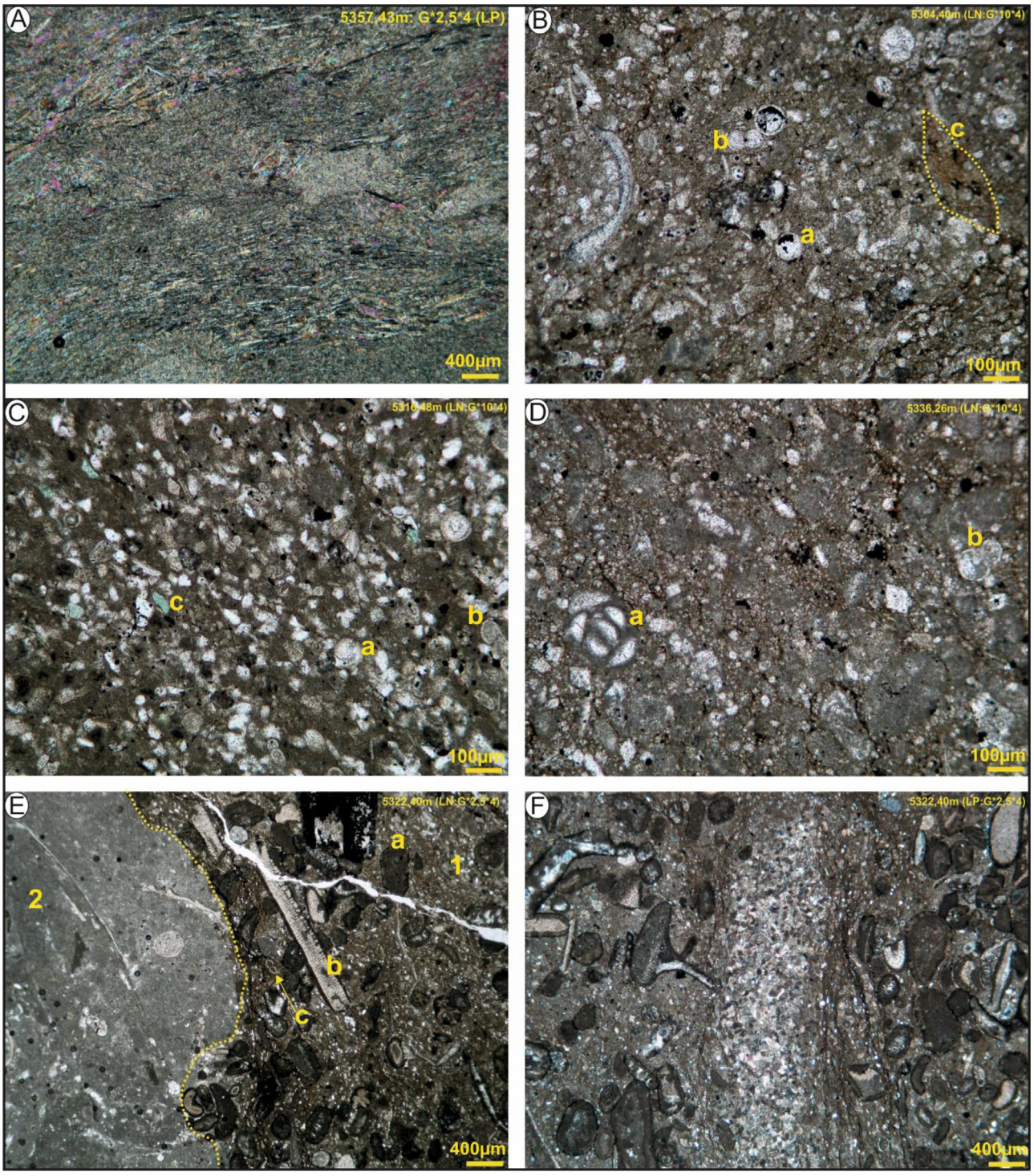

Fig. 7. The fine facies grained of the Douleb Member (Units U2 and U3). A: (Mf10) Anhydrite facies. B: (Mf4) Stylolitic packstone with calcispheres (a) and planktonic foraminifera (b), the calcispheres are filled with pyrite, (c) phosphatization of the matrix. C: (Mf12) Sandy packstone with calcispheres (a) and planktonic foraminifera (b), quartz (c). D: (Mf5) Stylolitic packstone with miliolids (a), benthic and planktonic foraminifera (b), phosphatisation (c). E: (Mf8) Two microfacies: 1 a stylolitic packstone rich in oolites (a), echinoderms (b), planktonic foraminifera (c), gastropods and micritized bioclasts, 2 wackestone-packstone rich in echinoderms and foraminifers. F: (Mf8) Oolitic packstone intercalated by a grainstone texture microfacies with small pellets (a) and stylolites (b).

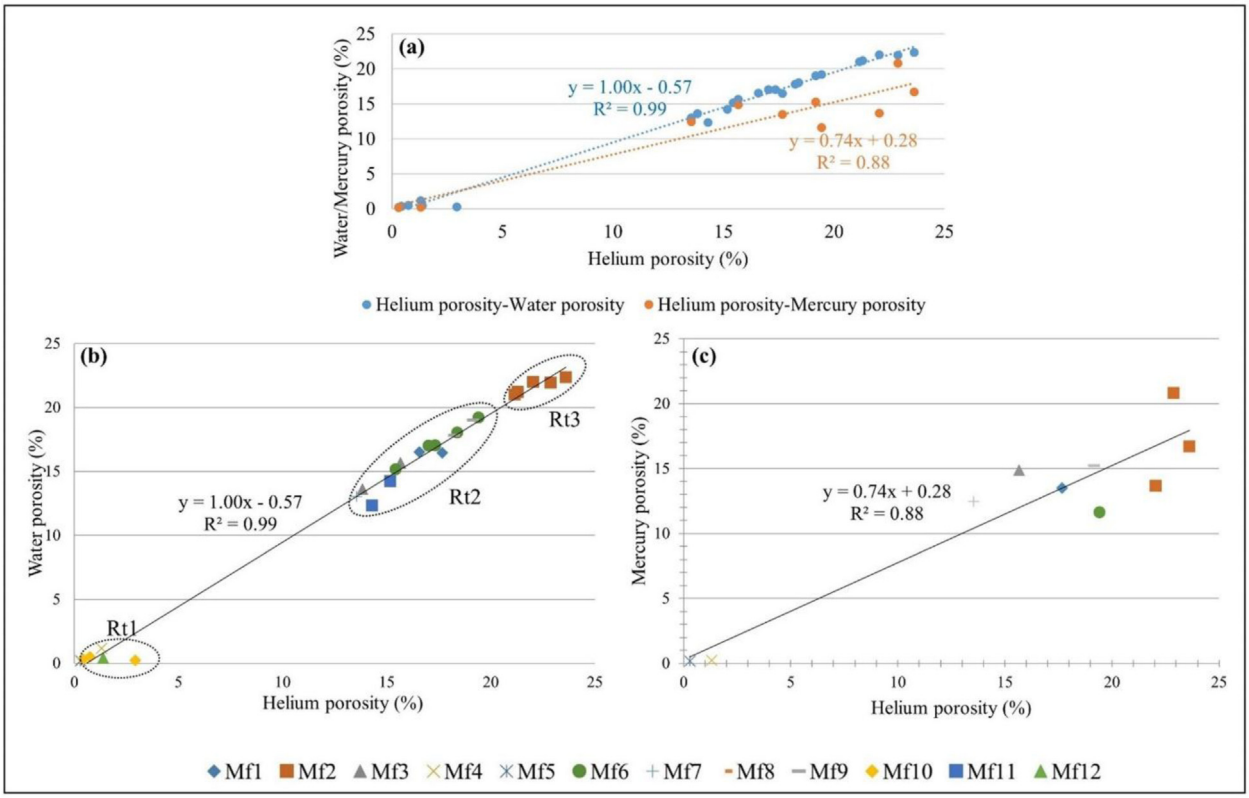

Legend:

- Mf1: dolomitized packstone rich in rudists
- Mf2: fine grainstone with small peloids, rudists and some benthic foraminifera
- Mf3: packstone-grainstone with small rudist-debris, echinoderms and peloids
- Mf4: packstone with calcispheres, planktonic foraminifera and some debris
- Mf5: packstone with miliolids, ostracods, benthic foraminifera and peloids
- Mf6: packstone with large rudists, peloids and some intraclasts
- Mf7: wackestone with fragmented rudists
- Mf8: packstone with oolites, micritized bioclasts, echinoderms, gastropods and benthic foraminifera
- Mf9: dolomite
- Mf10: Anhydrite
- Mf11: packstone with peloids, some benthic foraminifera and echinoderm debris
- Mf12: sandy wackestone with calcispheres, rare planktonic foraminifera and some intraclasts

Fig. 8. Water porosity and mercury porosity versus helium porosity.

Table 2. Results obtained for the porosity measured by mercury injection.

Sample ID	Microfacies	CP (%)	TrP (%)	FP (%)	d1 (μm)	d2 (μm)	ST (μm)	AP (μm)
2	Mf1	13.50	9.90	3.60	20	0.30	19.70	4
5	Mf2	16.70	10.70	6.00	10	0.60	9.40	3
16	Mf6	11.63	8.83	2.80	200	0.20	199.80	15
17	Mf7	12.47	9.67	2.80	6	1.00	5.00	3
20	Mf9	15.24	12.84	2.40	100	0.20	98.00	15

CP: connected porosity; TrP: trapped porosity; FP: free porosity; d1: injection start diameter; d2: end diameter of the injection; ST: spreading of threshold; AP: average pore.

smaller than those used in the other two techniques (water and helium saturation) which may have induced some uncertainty and therefore resulted into dispersion of the data (Bertrand *et al.*, 2021).

Because of the homogeneity of the results obtained by water and helium saturation, to discuss the correlation with the other petrophysical parameters (density, permeability, P-waves velocity and thermal conductivity), only the porosity measured by helium saturation will be taken into consideration to draw relationship with other properties.

4.2.1.2 Pore throat distribution

The Hg-porosimetry gives valuable data about the pore volume distribution according to the access thresholds or pore diameters distribution, the percolation threshold (Katz and Thompson, 1986) are ranging from 3 to 15 μm (Tab. 2; Fig. 9). However, this relative homogeneity of this parameter covers an important variation of the injection curve shapes illustrated by the spreading between d1 and d2 values. According to the classification of Ali *et al.* (2010), the main part of the porosity is defined as mesopores and macropores (Tab. 3). Three types of samples show a small fraction of micropores, Mf6, Mf1 and Mf2 (Tab. 3; Figs. 9A', 9C' and 9D'). The spreading of the pore throats becomes tighter when the grain sorting is better.

A large distribution (ST: 199.8 μm) is observed for the facies Mf6 (Fig. 9A), its texture is packstone-grainstone with peloids and rudists. It is very poorly sorted facies with debris of variable sizes. On the other hand, Mf1, Mf2 and Mf7 facies are well-sorted rudist-rich facies with a ST ranging between 5 and 19.7 μm.

The pore throat distribution could be divided in several pore families according to its wideness and its segmentation. Three classes for the poorly sorted material (Mf6, Fig. 9A'), dolomitized material (Mf9, Fig. 9B'), two classes for the more sorted material (Mf1 and Mf2, Figs. 9C' and 9D') and one class for the well sorted one (Mf7, Fig. 9E').

The trapped porosity (TrP; Fig. 9), calculated for threshold lower than 6 μm (see Sect. 3.2.1.3), remains relatively high (50% and more). These values demonstrate a strong porosity shape heterogeneity, ink-bottle shapes, for the meso- and micropore network due to the heterogeneity of the sediment granulometry.

Thus, dispersion of the pore throat size increases from the wackestone to the packstone passing through the group of dolomitized samples. The percolation threshold ranges over less than one order of magnitude from 3 to 15 μm whereas the wideness of the pore size distribution ranges over more four orders of magnitude from 0.1 μm to more than 200 μm for the packstone. The threshold spreading is clearly dependent on the spreading of the clasts' size.

4.2.2 Permeability

The three rock-types considered previously using helium porosity and facies criteria have specific nitrogen permeability properties (Fig. 10).

- The Rt1, characterized by samples with low permeability and porosity, with anhydrite (Mf10), wackestones (Mf12) and packstones (Mf4, Mf5 and Mf8). Their very low porosity induces a very low connectivity of the porous network and then of their low permeability.
- The Rt2, with, Mf1, Mf3, Mf6, Mf7, Mf9 and Mf11 facies shows an intermediate porosity from 14 to 20%, and a large dispersion of the permeability values from 0.9 to 3760 mD. This large distribution is not only linked to the porosity variation but depends on the percolation threshold value and on the wideness of the threshold distribution, probably significant of connectivity variations (Nooruddin *et al.*, 2014; Mielke *et al.*, 2017). In this way, the permeability decreases with the percolation threshold value and with the wideness of the pore throats distribution illustrates by the Mf6, Mf9, Mf1 and Mf7 facies (Fig. 9).
- The Rt3 composed of Mf2 samples (Figs. 6C and 6D), with the highest porosity (between 21 and 24%) but an intermediate permeability (between 21 and 360 mD) is controlled by an intermediate threshold wideness (Fig. 9).

These porosity-permeability relations are in accordance with the rock fabric-petrophysical classes proposed for the non-vuggy carbonate by Lucia (1999, 2004). They illustrate the grain size and textural dependences of these properties (Fig. 1-2.20 in Zinszner and Pellerin, 2007). Measured values are in the same range than values obtained by Soete *et al.* (2015) or Watanabe *et al.* (2019) but higher than measured values on Lebanon samples by Salah *et al.* (2020). The correlation coefficient is quite good considering the facies variability.

4.2.3 Bulk density

The data set ranges over 2.65 and 2.45 $g.cm^{-3}$ for volumetric mass density. The main correlation line with porosity, well drawn for the calcite materials, demonstrates the absence or the very low amount of unconnected porosity for

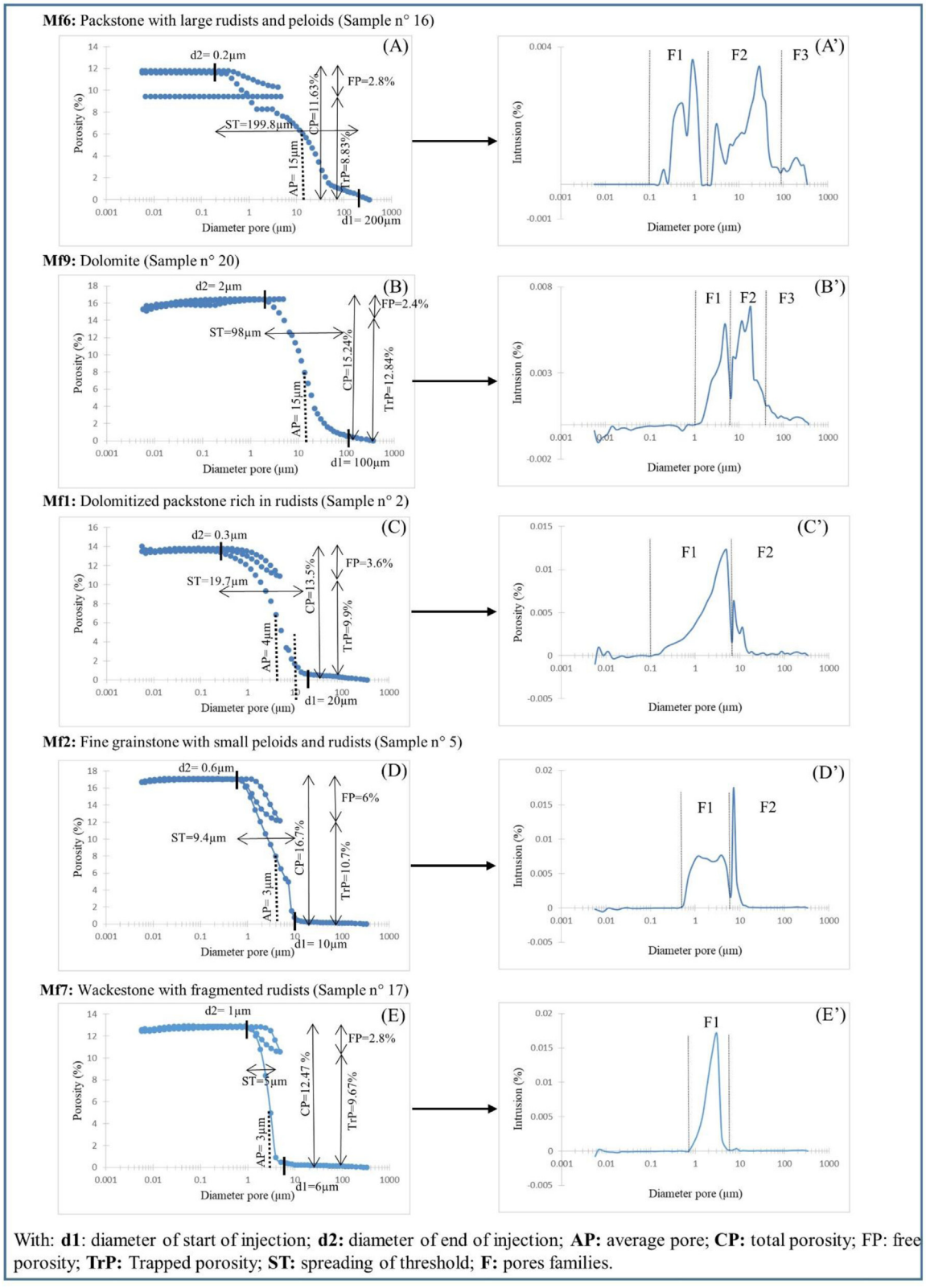

Fig. 9. Pore throat distribution curves obtained from mercury injection capillary pressure tests.

Table 3. Number and types of pores obtained by mercury injection (Based on the classification of Al-Marzouqi *et al.*, 2010).

Samples ID	Microfacies	Number of pores (families types)	Pores family	Types of pores	Average pore for each family
2	Mf9	3	F1: 1–7 μm	F1: mesopores and macropores	F1: 5 μm
			F2: 7–40 μm	F2: macropores	F2: 20 μm
			F3: 40–400 μm	F3: macropores	F3: 200 μm
5	Mf6	3	F1: 0.2–2 μm	F1: micropores and mesopores	F1: 1 μm
			F2: 2–90 μm	F2: micro, meso and macropores	F2: 30 μm
			F3: 90–350 μm	F3: macropores	F3: 200 μm
16	Mf2	2	F1: 0.4–6 μm	F1: micro, meso and macropores	F1: 2 μm
			F2: 6–10 μm	F2: macropores	F2: 7 μm
17	Mf1	3	F1: 0.1–8 μm	F1: micro, meso and macropores	F1: 5 μm
			F2: 8–30 μm	F2: macropores	F2: 8 μm
20	Mf7	1	0.7–7 μm	mesopores and macropres	3 μm

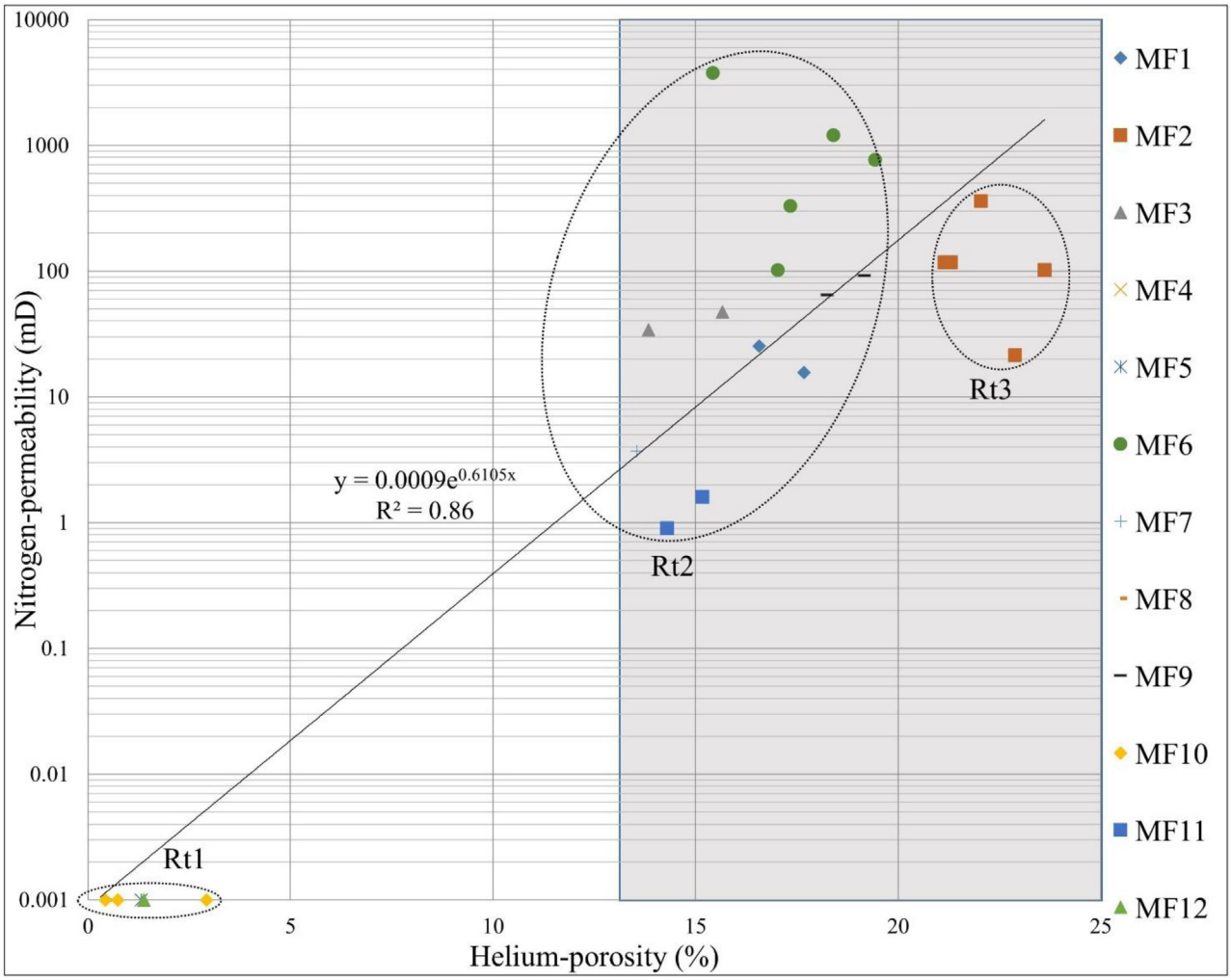

Fig. 10. Permeability *versus* helium porosity.

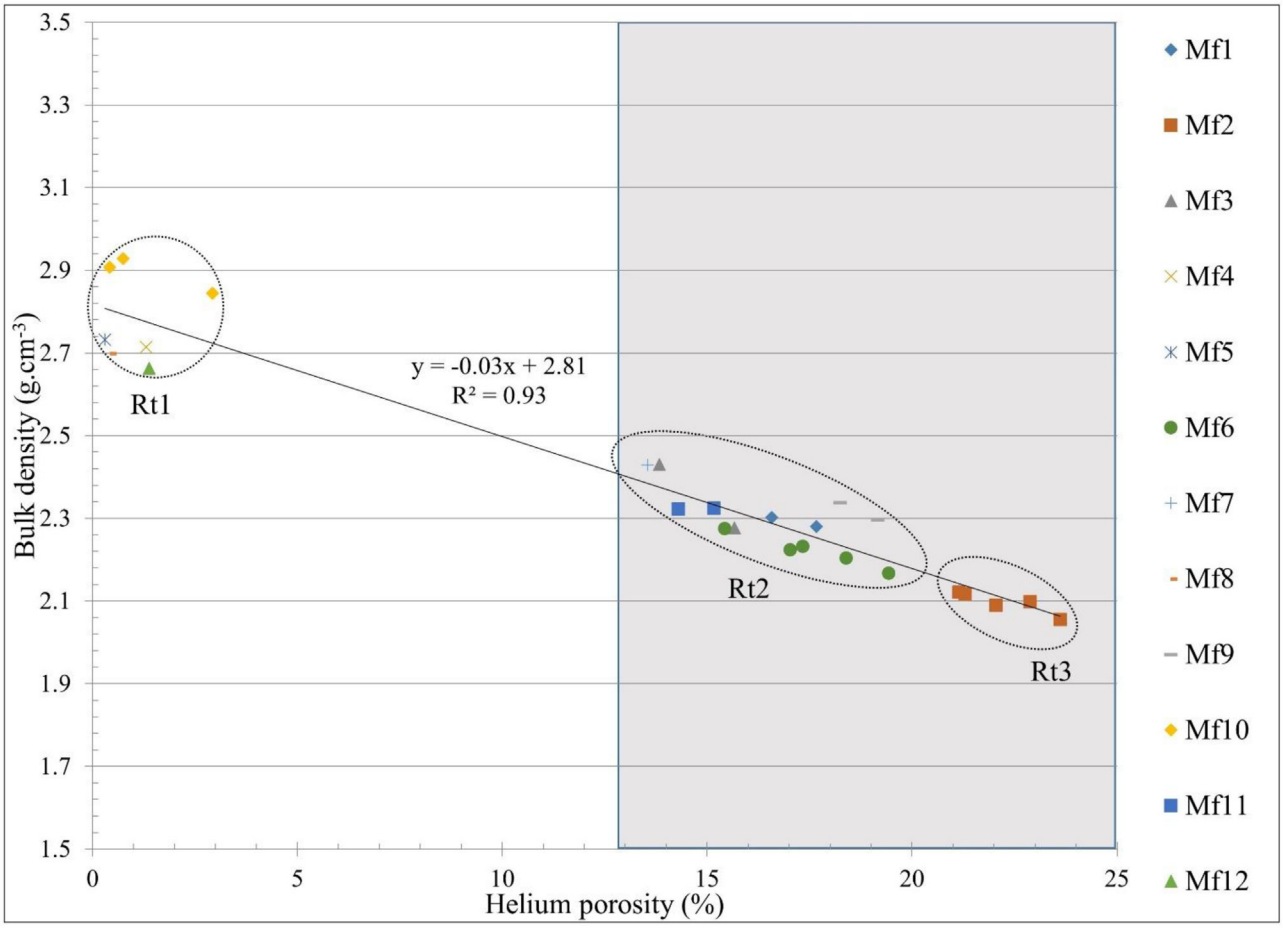

Fig. 11. Bulk density *versus* helium porosity.

samples below the correlation line, especially for the low porosity samples (Fig. 11). The samples above the correlation line are clearly mixed samples with a low fraction of dolomite or anhydrite.

4.2.4 P-waves velocity

The P-waves velocity range from 2060 to 6094 m.s^{-1}. It presents a quasi-linear distribution regarding to the porosity (Fig. 12). These values are consistent with the results obtained by Fournier *et al.* (2014), Mielke *et al.* (2017), Bailly *et al.* (2019) or Salah *et al.* (2020). For each Rt, dispersion around the mean line is the conjugate effect of grain size, the type of contact between grains, void shape and microfractures.

The Rt1 group, those with speed ranging from 5063 to 6094 m.s^{-1} and porosity, lower than 4% is formed by microfacies Mf4, Mf5, Mf8, Mf12, and the increase of the P-wave velocity dues to a decrease of the matrix content (Figs. 7B–7E, respectively). In this group of low porosity, anhydrite samples (Mf10, Fig. 7A) present a large set of planar structures that could explain the important variability of the P-waves.

The Rt2 group, with porosity from 14 to 19%, and P-wave velocity from 2364 to 4762 m.s^{-1} is formed by Mf1, Mf3, Mf11, Mf7, Mf9 and Mf6 microfacies and ordered with increasing P-wave velocity. This order illustrated the effect of the contact shape from punctual and discontinuous planar from Mf6 (Figs. 13A and 14A) and, planar and continuous for the others. Mf1 and Mf9 facies are dolomitic, with grains constituting a rigid network useful for P-wave propagation (Figs. 6B, 13B and 14B), these facies representative of the main behavior. The dolomite content does not induce significant variation of the P-wave velocity as already proposed by Verwer *et al.* (2011).

The Rt3 group is composed of Mf2 samples. Porosity values vary from 21 to 24% and velocities from 2060 to 2797 m.s^{-1}. Samples of this group presents a large degree of cementation and associated change of the porosity shape (Figs. 6C, 13C and 13D).

Fournier *et al.* (2014) calculated P-wave velocity/porosity relationship involving pore shape, pore shape of their samples ranges from 0.1 and 0.2. These values are acquired under 40 MPa confining pressure. Concerning the Tunisian samples taken for this study, porosity ranges from 12 and 13%, while the P-wave velocity ranges from 4200 and 2000 m.s^{-1}, measured under atmospheric conditions, similar data are obtained by Salah *et al.* (2020). Using the Figure 8a of Fournier *et al.* (2014), the inclusion aspect ratio of the porosity ranges from 0.1 and 0.05 corresponding to a flatter pore shape. Pore shape difference could be linked to difference in experimental

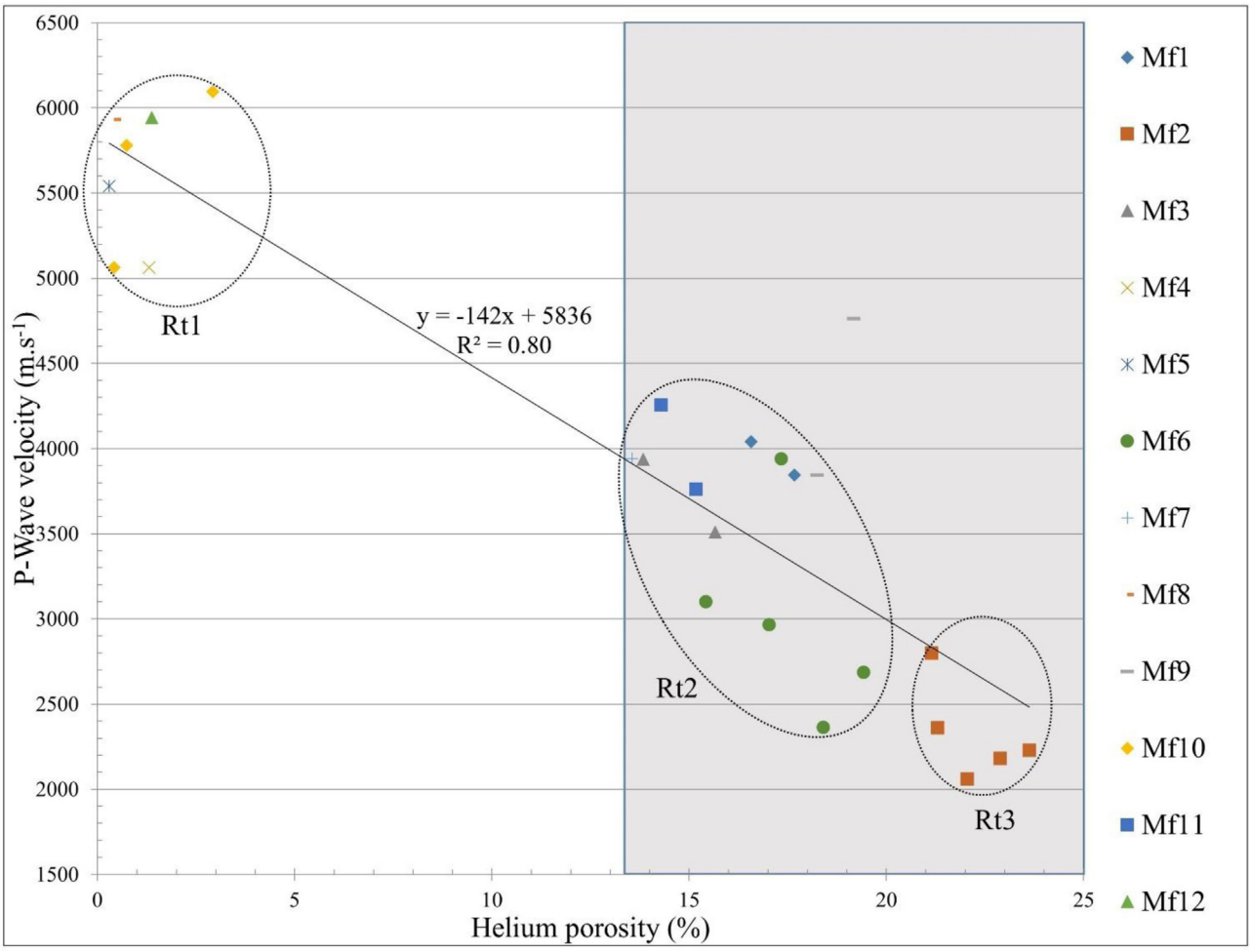

Fig. 12. P-wave velocity *versus* helium porosity.

conditions, and in particular the confining pressure difference. Indeed, P-wave velocity increases for measurements performed under low confining pressure range and this increase is attributed to closing of micro-cracks (Gardner *et al.*, 1974; Vernik, 1994), but microcracks are not observed in thin-sections, only stylolithes are present in numbers and could explain the variability if they are opened, but interpretation of these petrophysical values remains subject to discussion.

4.2.5 Thermal conductivity

Thermal conductivity values range from 1.4 to 3.8 $W.m^{-1}.K^{-1}$ (Fig. 15). This result is consistent with data found in the bibliography (Hartmann *et al.*, 2005; Pasquale *et al.*, 2015; Mielke *et al.*, 2017). The facies Mf10, presents the highest value due to the high thermal conductivity of the Anhydrite (around 5 $W.m^{-1}.K^{-1}$, Clauser and Huenges, 1995; Pasquale *et al.*, 2015) with regard to calcite one (3.5 ± 0.5 $W.m^{-1}.K^{-1}$; Clauser and Huenges, 1995) and the low porosity of the material. Similar analysis is made for facies Mf9 with high dolomite content, indeed, the thermal conductivity of dolomite is 4.8 ± 0.54 $W.m^{-1}.K^{-1}$ (Clauser and Huenges, 1995; Pasquale *et al.*, 2015), while the relative lowest value of the facies Mf5, dolomite also, is attribute to the more dispersed dolomite grains than in MF9.

Except these previous facies, Figure 15 deciphers a sharp control of the porosity on this property for the other calcite facies. It seems that the thermal conductivity is less sensitive to the shape of the porous network and to the grain contact than P-wave velocities.

5 Petrophysical properties and rock-types characteristics

The twelve microfacies are gathered in three groups of facies, they have their own petrophysical and sedimentological characteristics.

5.1 The first rock-type (Rt1)

Samples of the first group Rt1 show the lowest porosity and permeability values and the highest P-wave velocity and thermal conductivity values. These properties depend on their low porosity and high density, themselves controlled by sedimentological and diagenetic processes (Salah *et al.*, 2016; Njahi *et al.*, 2017; Corbett *et al.*, 2017). They regroup the lowest porous microfacies including Mf4, Mf5, Mf8, Mf10 and Mf12.

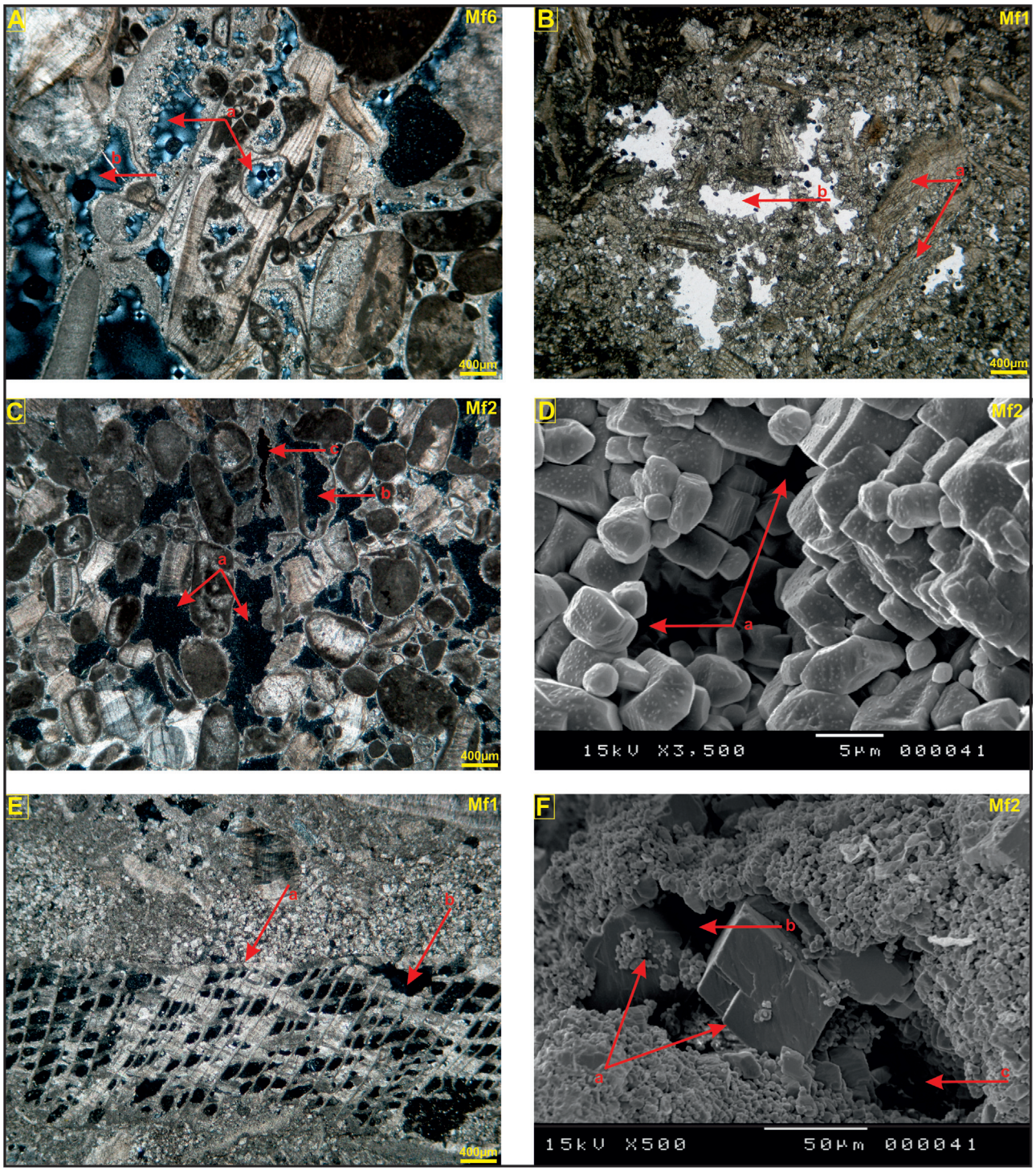

Fig. 13. The different types of porosity characterizing the Douleb reservoir. A: (Mf6) An intragranular (a) and intergranular (b) porosities observed between rudists. B: (Mf1) Rudist-rich packstone of Hippuritidae type (a) showing an important intergranular porosity (b). C: (Mf2) Packstone-grainstone with small rudist fragments and peloids showing an intergranular (a) and intragranular (b) porosity and oil-impregnation (c). D: (Mf2) SEM photography showing the matrix porosity (a) in fine grainstones with small debris of rudists and peloids. E: (Mf1) Radiolitidae type rudist (a) showing an important intragranular porosity (b). F: (Mf2) SEM photograph shows matrix (a) and intercrystalline porosity (b) between dolomite crystals (c).

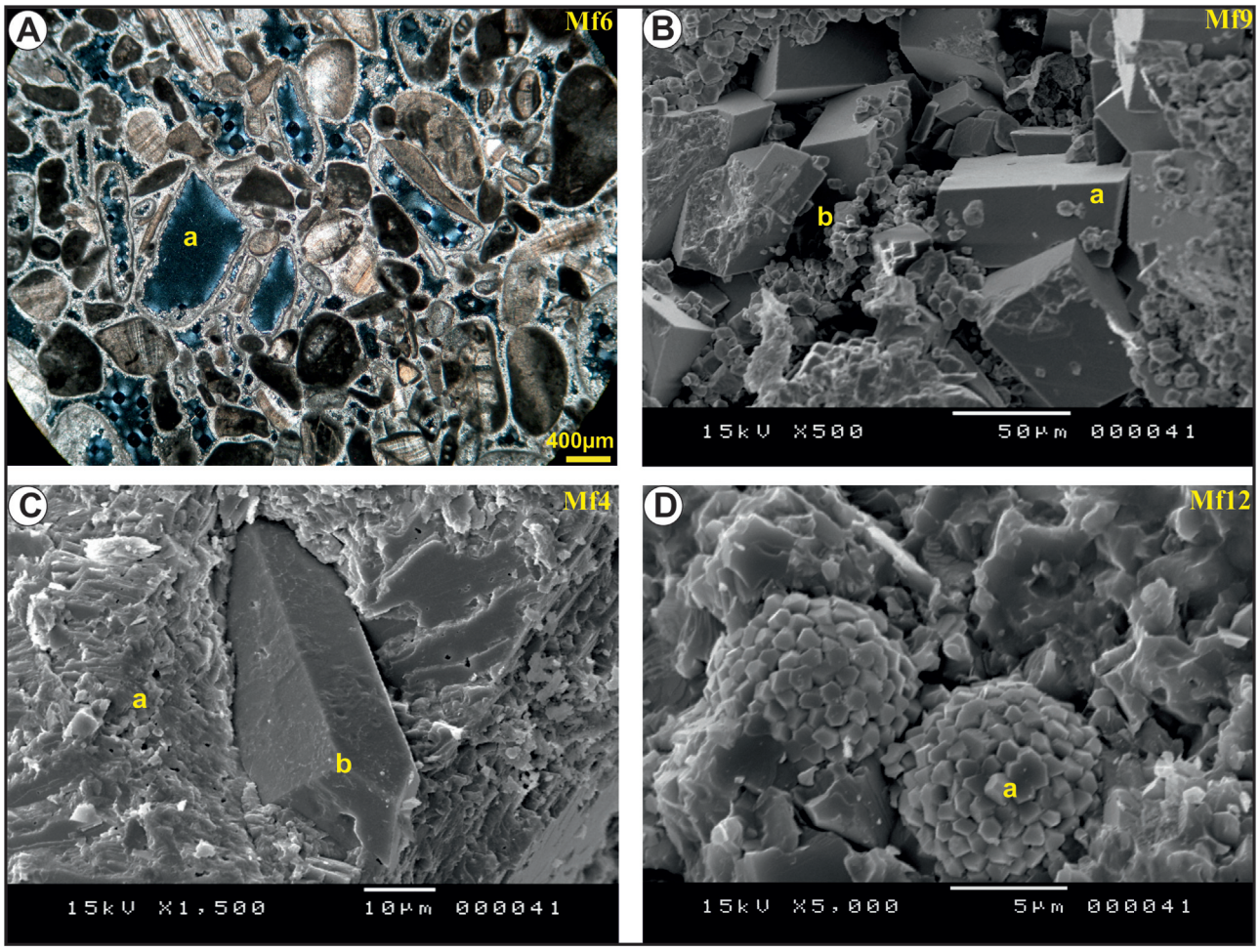

Fig. 14. The main diagenetic processes affecting the Douleb reservoir. A: (Mf6) Dissolution of bioclasts and genesis of secondary porosity (a) in coarse rudist debris and peloids facies. B: (Mf9) Matrix dolomitization (a): Development of intercristalline porosity (b). C: (Mf4) Silicification of the compacted micritic matrix (a): the pores are filled by hexagonal quartz crystals (b). D: (Mf12) filling of pores with framboidal pyrite (a).

According to their density and mineral composition, two sets of samples are recognized. Those with a calcite composition, correspond to the fine micritic units rich in quartz (Fig. 14C), sulfures (Fig. 14D), phosphates and glauconite, and those with an anhydrite composition and a higher solid phase density.

The fine-grained micritic microfacies (Mf4, Mf5, Mf8, Mf10 and Mf11; Figs. 7A–7E), are mainly composed of oolites, peloids, gastropods, foraminifers and calcispheres. These facies are belonging to the U2 and U3 units of the Douleb Member. These facies are affected by strong compaction with development of numerous stratiform stylolithes (Figs. 5I, 7B and 7D–7F). The dissolved mater precipitates nearby around allochems and strongly reduces the porosity (Purser, 1975; Troudi, 1998).

Several facies (Mf4, Mf5, Mf8 and Mf12) are also affected by a silicification of the matrix with hexagonal-shaped automorphic quartz crystals (Fig. 14C), by precipitation of pyrite (Fig. 14D) and phosphates (Fig. 7B) decreasing the porosity of these facies. They explained mainly the highest thermal conductivity values. The pore threshold of fine-grained facies initially low at sediment deposition is reduced by diagenetic processes. So, the low permeability is likely related to their low porosity (from 0.3 to 2.9%), their low threshold values and small induced percolation threshold (Nooruddin *et al.*, 2014).

In the Rt1, P-wave velocity values, result from the low porosity however, measured values are lower than the pure mineral one (Tab. 2S; see Supplementary Material). The gap between these values, signs up the clay content and the shape of the contact between grains (Fournier *et al.*, 2014).

The anhydrite facies are related to high values for P-wave and thermal conductivity properties due to textural effects and the high properties of the constituting minerals.

5.2 The second rock-type (Rt2)

The Rt2 comprising Mf1, Mf3, Mf6, Mf7, Mf9 and Mf11 facies with intermediate porosity and density values, are mainly bioclastic carbonates (mostly formed by rudists), of Hyppuritidae (Figs. 13A and 13B) and Radiolitidae type (Figs. 6E and 13E). The dolomitic facies (Mf9) present slightly

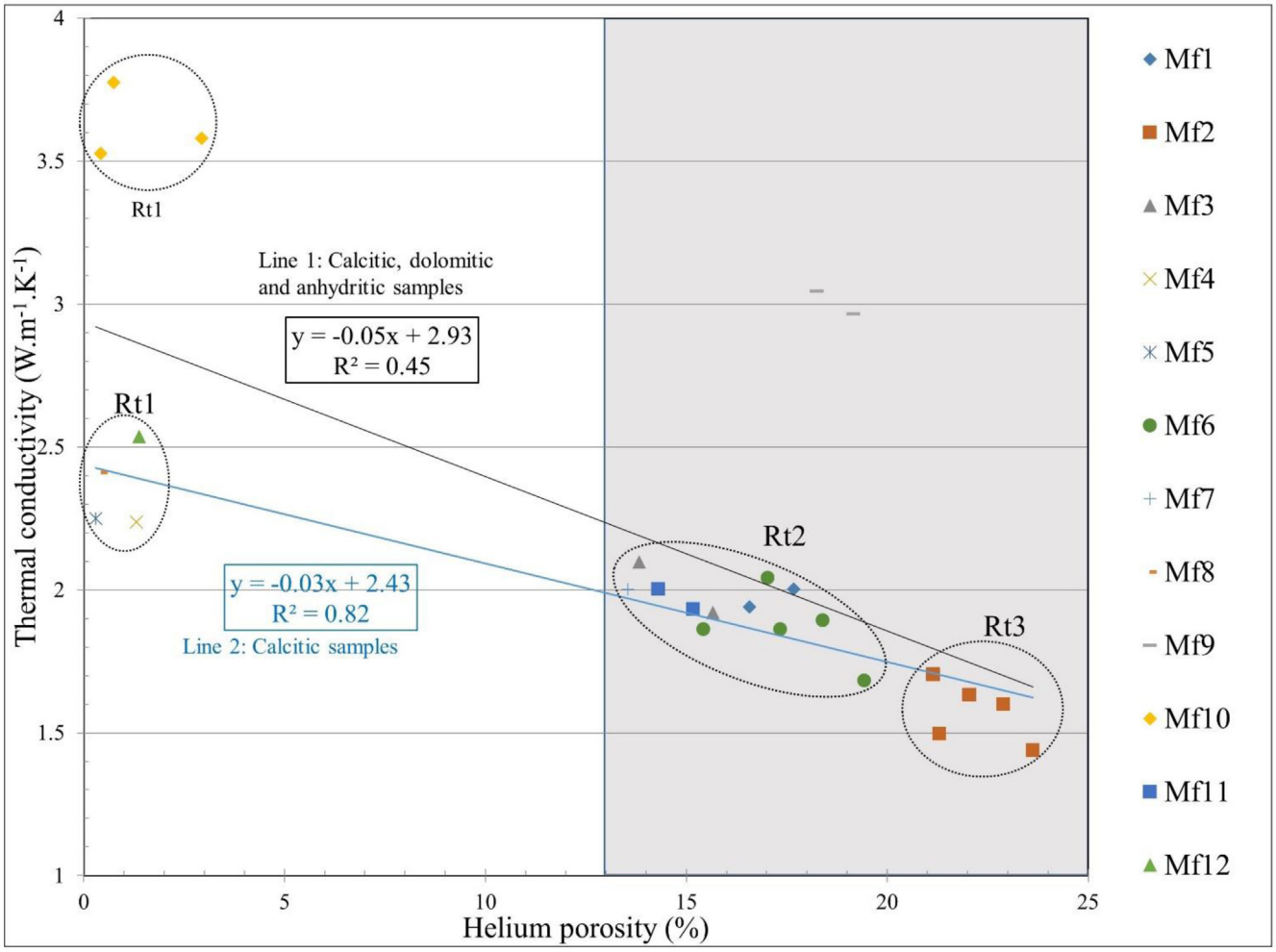

Fig. 15. Thermal conductivity *versus* helium porosity.

different values. This group is formed by the oil-impregnated bioclastic facies presenting a medium to good reservoir quality (*i.e.* porosity and permeability values).

Variations of the bioclast size and matrix content clearly control the wideness of the threshold distribution directly linked to the high permeability values and to the low P-wave velocity and thermal conductivity values. The permeability increases with the percolation thresholds values and with the widening of the throat wideness (Fig. 16) (Ehnenberg *et al.*, 2006; Rashid *et al.*, 2015; El Husseiny and Vanorio, 2016). Dolomitic facies have specific comportment; the permeability is low while the percolation threshold and the wideness of the throats are high like those of high permeability samples highlighting a role of the pore shapes specific for these facies.

A relationship between these parameters is classically described (Katz and Thompson, 1986) even if other parameters (tortuosity, fractal tubular bundle) may act an important function (Buiting and Clerke, 2013; Rashid *et al.*, 2015). The combined effect of both parameters is illustrated by le Mf11 samples suite, where the permeability increases with increase of the percolation threshold (average pore: AP) and throat wideness. The enlargement of the pore threshold distribution is linked to the increase of grain size dispersion and especially for the Mf6 facies, with a crack network development.

Limestones with large debris of rudists and peloids (Mf6) are characterized by low to medium velocity (between 2364 and 3939 $m.s^{-1}$) and medium to high porosity (between 15 and 19%). Variations of velocities and porosity are the results of badly-sorted grain sizes. The presence of dolomite and anhydrite in the samples leads to an increase in properties (thermal conductivity, and P-wave velocity) due to both the properties of the minerals and the nature of the contact between the grains.

5.3 The third rock-type (Rt3)

The Rt3 regroups Mf2 facies samples, with the highest porosity and the lowest bulk density. They are the grainstones with small rudists and peloids, corresponding to the most porous oil-soaked facies.

This rock-type is formed by single facies with well-sorted small rudist-debris and peloids (Mf2). The porosity is qualified as high to very high. It is a very well classed facies: well-sorted small grains showing matrix porosity (Figs. 13D and 13F), intra/intergranular (Fig. 13C) and intercrystal porosity (Fig. 13F).

Microscopic study has shown that Rt3 facies, as Rt2, are mainly affected by dissolution (Fig. 14A) and matrix

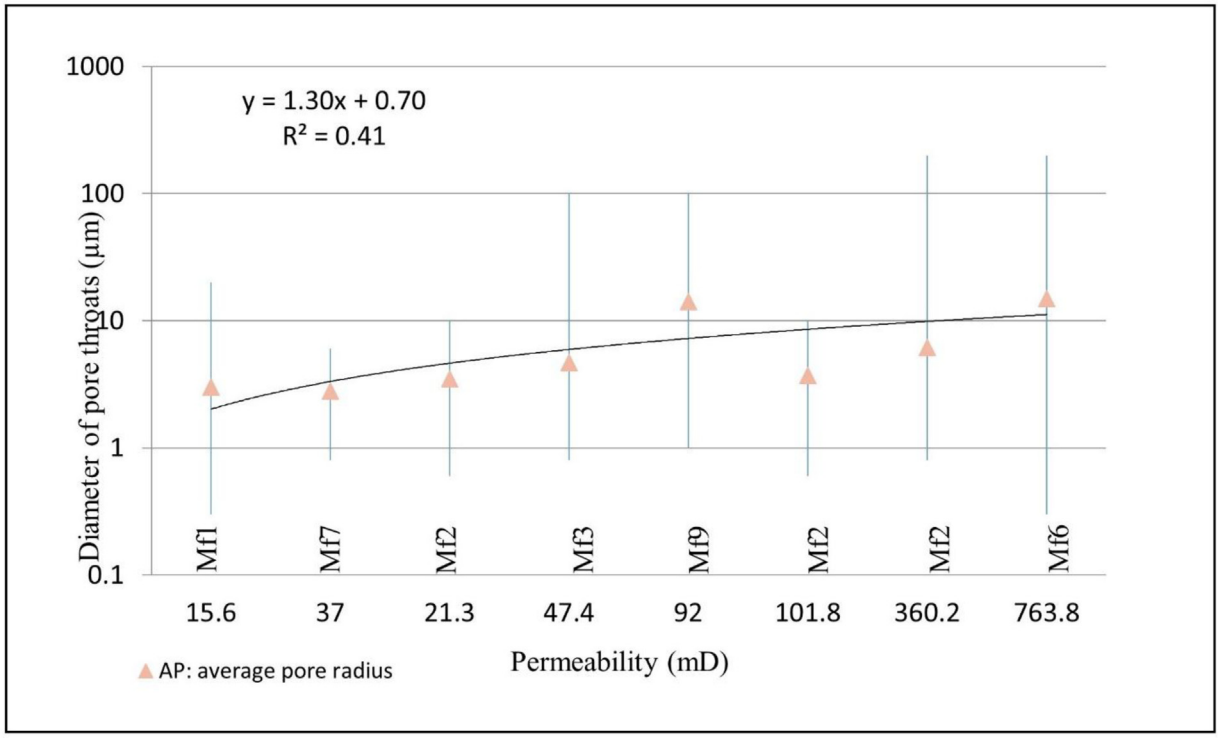

Fig. 16. Average diameter of pore throats *versus* permeability.

dolomitization (Fig. 13F) that create a significant secondary porosity (intercrystal or moldic). Although these samples have the highest porosity, their permeability is intermediate from 10 mD to 1 D. These transfer properties are correlated to the intermediate threshold sizes. The lowest values of P-wave velocity (2324 $m.s^{-1}$ on average) and thermal conductivity (lower than 1.8 $W.m^{-1}.K^{-1}$), are obtained in the most porous facies (Mf2) corresponding to grainstones containing small sized and well sorted peloids and rudists (Wyllie *et al.*, 1958).

6 Vertical evolution of petrophysical parameters

Petrophysical parameters (porosity, permeability, P-wave velocity, and thermal conductivity) measured on 26 samples all along the core, are shown in Figure 17. The representative samples of each microfacies defined in the study, have the same petrophysical properties, all along the studied interval, regardless of the depth, which means that there is no effect of the burial on these properties:

- Fine micritic facies (Mf4, Mf5, Mf8 and Mf12) and anhydrites facies (Mf10) show low porosity, very low permeability, very high P-wave velocity, and high thermal conductivity.
- Facies with small and well-sorted rudist debris and peloids (Mf2) always show very high porosity, high permeability, low P-wave velocity, and low thermal conductivity.
- Facies with small rudist debris, echinoderms and peloids (Mf3) have average values of porosity, permeability, P-wave velocity, and thermal conductivity.
- The facies with large debris of rudists and peloids (Mf6) generally show good porosity, high to excellent permeability notably in fractured units, an average P-wave, and thermal conductivity values.
- Finally, the dolomite facies (Mf9) show high values of porosity, permeability, and thermal conductivity. However, the velocity of the P-wave is variable, it is fair when the facies are filled with small crystals of anhydrite and becomes higher when the facies contains only dolomite (Lucia, 2004; Ehnenberg *et al.*, 2006).

These different laboratory analyses carried out on the rocks allow us to have an idea about the behaviour of the petrophysical properties of underground rocks and to propose hypotheses concerning the favourable location of the organic matter in the sub-surface. So, it is recommended to pay a particular attention to layers characterized by low P-wave velocity, low density and low thermal conductivity. These declines are usually associated to good porosity values (Tab. 4).

7 Conclusion

This study concerns a reservoir level well known in Cretaceous formations and focuses on an interval of about 112 m. Samples from the existing reservoir were collected

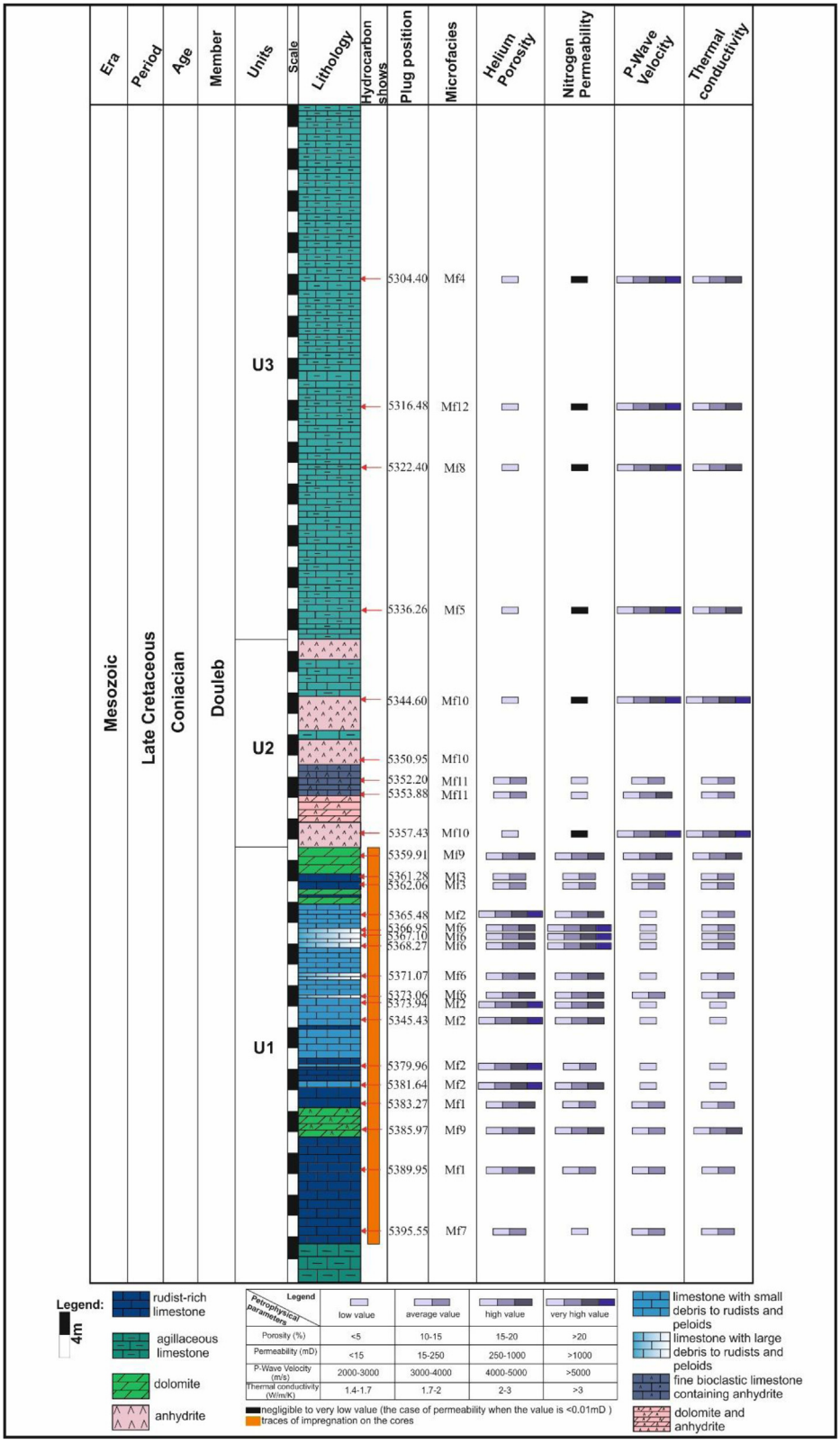

Fig. 17. Evolution of petrophysical parameters as a function of depth and facies types of limestones.

Table 4. Summary table on the relationship between the different petrophysical parameters measured.

Porosity	Permeability	Density	P-Wave Velocity	Thermal conductivity	Microfacies
⇧	⇧	⇩	⇩	⇩	Mf1, Mf2, Mf3, Mf6, Mf7, Mf9
⇧	⇩	⇩	⇩	⇩	Mf11
⇩	⇩	⇧	⇧	⇧	Mf4, Mf5, Mf8, Mf10, Mf12

With: ⇧ increase ⇩ decrease

by drilling and characterized after washing the hydrocarbons. The measured properties (permeability, thermal conductivity, and P-wave velocity) are compared with the characteristics of the materials (petrography, granulometry, porosity, size of access to voids).

From a petroleum perspective and based on petrophysical analyses, it appears that only facies found in rock-types Rt2 and Rt3 belonging to the first unit (U1) are oil-impregnated (according to the macroscopic study). They have a petroleum interest and can be considered as a reservoir layer. These facies consist of dolomites (Mf9), wackestones-packstones and grainstones rich in rudists (Mf1, Mf2, Mf3, Mf6 and Mf7). In this unit, the rock-type Rt2 regroups fine grainstones containing small and well sorted rudist-debris and peloids (Mf2) and shows the best petrophysical characteristics (porosity and permeability).

The obtained results show a strong influence of the granulometric dispersion, due to sedimentological origin and to diagenetic dolomitization, of the pore volume and of the width of the distribution of the access thresholds. These two characteristics and the percolation threshold exert an important control on permeability. The two other measured properties are mainly controlled by their mineralogical and porosity contents. Their lower measured values than the calculated one illustrated a strong control of the contact properties as well for transfer of thermal fluxes or elastic stresses. Determination of these characteristics, partly depending on the pore shapes that influence the permeability too, could be the next step of analysis to understanding the links between material characteristics and their transfer properties.

Supplementary Material

Figure 1S. Integrated sedimentological and petrophysical analysis workflow for Douleb carbonate reservoir study.
Table 1S. Petrophysical properties of the studied sequence.
Table 2S. P-wave velocity and thermal conductivity of minerals (Clauser and Huenges, 1995).

The Supplementary Material is available at http://www.bsgf.fr/10.1051/bsgf/2022020/olm.

Acknowledgments. This paper is a contribution to the Cooperative Program between the Universities of Lorraine (France) and Tunis El Manar (Tunisia) CMCU 13G1003-PHC 28533TJ, and part of the PhD of the first author. We are grateful to the reviewers who contributed to the improvement of this paper.
We express our sincere thanks to ETAP (Entreprise Tunisienne d'Activités Pétrolières) for allowing the publication of these results.

References

Abdallah H, Sassi S, Meister C, Souissi R. 2000. Stratigraphie intégrée et paléogéographie des séries sédimentaires à la limite Cénomanien-Turonien dans la région Gafsa-Chotts (Tunisie centrale). *Cretaceous Research* 21: 35–106.
Al-Marzouqi M, Budebeds S, Sultan E. 2010. Resolving carbonate complexity. *Oilfield Review, Schlumberger* 22(2): 40–55.
Al-Tooqi S, Ehrenberg SN, Al-Habsi N, Al-Shukaili M. 2014. Reservoir rock typing of Upper Shu'aiba limestones, northwestern Oman. *Petroleum Geoscience* 20(4): 339–352.
Ali SA, Clark WJ, Ray Moore W, Dribus JR. 2010. Diagenesis and reservoir quality. *Oilfield Review, Schlumberger* 22(2): 14–27.
Bachari M, Grosheny D, Ferry S, France-Lanord C, Negra MG. 2019. The Cenomanian-Turonian Boundary Event (CTBE) in north-central Tunisia (Jebels Serj and Bargou) integrated into regional data (Algeria to Tunisia). *Cretaceous Research* 94: 108–125.
Bailly C, Fortin J, Adelinet M, Hamon Y. 2019. Upscaling of elastic properties in carbonates: A modeling approach based on a multiscale geophysical data set. *Journal of Geophysical Research: Solid Earth* 124(12): 13021–13038.
Belikov BP. 1967. Plastic constants of rock-forming minerals and their effect on the elasticity of rocks. IPST, pp. 118–124.
Ben Ayed N. 1986. Évolution tectonique de l'avant-pays de la chaîne alpine de Tunisie du début de mésozoïque à l'actuel. Thèse d'État, Université de Paris-Sud, Orsay, France, 286 p.

Bertrand L, Géraud Y, Diraison M. 2021. Petrophysical properties in faulted basement rocks: Insights from outcropping analogues on the Western Rift shoulders. *Geothermics* 95: 102–144.

Bey S, Kuss J, Premoli Silva I, Negra MH, Gardin S. 2012. Fault-controlled stratigraphy of the Late Cretaceous Abiod Formation at Ain Medheker (Northeast Tunisia). *Cretaceous Research* 34: 10–25.

Boughalmi S. 2020. Sédimentologie et diagenèse des faciès d'intérêt pétrolier du Crétacé Supérieur (Turonien-Coniacien) dans la région de Sfax et dans le Golfe de Gabès. Thèse de Doctorat, Université de Tunis El Manar, Tunisia, 257 p.

Boughalmi S, Negra MH, Géraud Y, Grosheny D, Saïdi M. 2019. Reservoir properties of Turonian rudist-rich carbonates in Central Tunisia (the onshore of Sfax area). *Arabian Journal of Geosciences* 12(15): 1–14.

Boulanouar A, Rahmouni A, Boukalouch M, Samaouali A, Géraud Y, Harnafi M, Sebbani J. 2013. Determination of thermal conductivity and porosity of building stone from ultrasonic velocity measurements. *Geomaterials* 3: 138–144.

Bourbié T, Coussy O, Zinszer B. 1986. Acoustiques des milieux poreux. Publication de l'Institut Français du Pétrole, 339 p.

Buiting JJM, Clerke EA. 2013. Permeability from porosimetry measurements: Derivation for a tortuous and fractal tubular bundle. *Journal of Petroleum Science and Engineering* 108: 267–278.

Burollet PF. 1956. Contribution à l'étude stratigraphique de la Tunisie centrale. Thèse Sc. Alger. *Ann. Min. Géol. Tunis* 18: 350.

Camoin G. 1989. Les plates-formes carbonatées du Turonien et du Sénonien de la Méditerranée centrale (Tunisie, Algérie, Sicile). Thèse de Doctorat d'État, Université Aix-Marseille, 242 p.

Caron M, Dall'Agnolo S, Accaire H, Barrera E, Kauffman EG, Amédro F, *et al.* 2006. High-resolution stratigraphy of the Cenomanian-Turonian boundary interval at Pueblo (USA) and wadi Bahloul (Tunisia): stable isotope and bio-events correlation. *Geobios* 39: 171–200.

Chaabouni M. 1996. The Bireno member excellent potential reservoir in central Tunisia. In: *10th Proceedings of Tunisia Petroleum Exploration & Production Conference, Tunisia, Entreprise Tunisienne d'Activités Pétrolières (ETAP)*, pp. 331–335.

Clauser C, Huenges E. 1995. Thermal conductivity of rocks and minerals. Handbook of physical constants. *American Geophysical Union (AGU)*: 105–126.

Corbett PWM, Wang H, Câmara RN, Tavares AC, Borghi De Almeida LF, Perosi F, *et al.* 2017. Using the porosity exponent (m) and pore-scale resistivity modelling to understand pore fabric types in coquinas (Barremian-Aptian) of the Morro do Chaves Formation, NE Brazil. *Marine and Petroleum Geology* 88: 628–647.

Denis A. 1990. Perméabilité de fracture et diagraphies acoustiques : traitements numériques de données obtenues en forage profond et sur modèle. Thèse de Doctorat, Université Bordeaux I, France, 174 p.

Dullien FAL. 1979. Porous media fluid transport and pore structure. Academic Press, 369 p.

Ehnenberg SN, Eberli GP, Keramati M, Moallemi SA. 2006. Porosity-permeability relationships in interlayered limestone-dolostone reservoirs. *American Association of Petroleum Geologists* 90(1): 91–114.

El Husseiny A, Vanorio T. 2016. Porosity-permeability relationship in dual-porosity carbonate analogs porosity-permeability of carbonates. *Geophysics* 82(1): MR65-MR74.

Fournier F, Léonide P, Kleipool L, Toullec R, Reijmer JJG, Borgomano J, *et al.* 2014. Pore space evolution and elastic properties of platform carbonates (Urgonian limestone, Barremian–Aptian, SE France). *Sedimentary Geology* 308: 1–17.

Gardner GHF, Gardner LW, Gregory RW. 1974. Formation velocity and density: The diagnostic basis for stratigraphic traps. *Geophysics* 39: 770–780.

Ghafoori M, Rastegarnia A, Lashkaripour GR. 2018. Estimation of static parameters based on dynamical and physical properties in limestone rocks. *Journal of African Earth Sciences* 137: 22–31.

Grasso M, Torelli L, Mazzoldi G. 1999. Cretaceous-Paleogene sedimentation patterns and structural evolution of the Tunisian shelf, offshore the Pelagian Islands (Central Mediterranean). *Tectonophysics* 315: 235–250.

Grosheny D, Ferry S, Jati M, Ouaja M, Bensalah M, Atrops F, *et al.* 2013. The Cenomanian-Turonian boundary on the Saharan Platform (Tunisia and Algeria). *Cretaceous Research* 42: 1–19.

Guéguen Y, Palciauskas V. 1992. Introduction à la physique des roches. Herman Edition, 299 p.

Haffen S, Géraud Y, Rosener M, Diraison M. 2017. Thermal conductivity and porosity maps for different materials: A combined case study of granite and sandstone. *Geothermics* 66: 143–150.

Hanini A, Zagrarni MF, Negra MH, Handoura M. 2004. The Cenomanian-Turonian Bahloul Formation in Central-North Tunisia. Biosedimentary events and hydrocarbon signification. In: *Proceedings of the 9th Tunisia Petroleum Exploration & Production Conference, Tunisia, Entreprise Tunisienne d'Activités Pétrolières (ETAP)*, pp. 73–83.

Hartmann A, Rath V, Clauser C. 2005. Thermal conductivity from core and well log data. *International Journal of Rock Mechanics and Mining Sciences* 42(7-8): 1042–1055.

Homand F, Duffaut P. 2000. Manuel de mécanique des roches. Paris : École des Mines, 265 p.

Jaballah J. 2017. Les séries du Crétacé supérieur (Albien-Campanien inférieur) en Tunisie centrale Méridionale. Caractères sédimentaires et intérêt économique. Thèse de Doctorat, Université de Tunis, Tunisia, 289 p.

Jaballah J, Negra MH. 2016. Stratigraphical and sedimentary characters of Late Cretaceous formations outcropping in central and southern Tunisia, Tethyan southern margin. *Journal of African Earth Sciences* 124: 289–310.

Katz AJ, Thompson AH. 1986. Quantitative prediction of permeability in porous rock. *Physical Review* 24: 8179–8181.

Khessibi M. 1978. Études géologiques du secteur de Maknassi-Mezzona et du Djebel Kébar (Tunisie centrale). Thèse de Doctorat, Université de Lyon, France, 175 p.

Klinkenberg LJ. 1941. The permeability of porous media to liquids and gases. Drilling and production practice. American Petroleum Institute, pp. 200–213.

Kloubek J. 1981. A new method for the investigation of porous structures using mercury porosimetry. *Powder Technology* 29: 89–97.

Lansari F, Troudi H, Negra MH. 2010. Outcrops-subsurface lithostratigraphic correlations of the Bireno carbonatic reservoir in Central Tunisia. In: *Proceedings of the 12th Tunisian Petroleum Exploration & Production Conference, Tunisia, Entreprise Tunisienne d'Activités Pétrolières (ETAP)*, pp. 63–69.

Lebedel V, Lézin C, Andreu B, Ettachfini ELM, Grosheny D. 2015. The upper Cenomanian-lower Turonian of the Preafrican trough (Morocco): Platform configuration and paleo environmental conditions. *Journal of African Earth Sciences* 106: 1–16.

Li Y, Wardlaw NC. 1986. The influence of wettability and critical pore-throat size ratio on snap-off. *Journal of Colloid and Interface Science* 109: 461–472.

Lucia FJ. 1999. Carbonate reservoir characterization. Berlin: Springer, 226 p.

Lucia FJ. 2004. Origin and petrophysics of dolostone pore space. In: Braithwaite CJR, Rizzi G, Darke G, eds. *The geometry and petrogenesis of dolomite hydrocarbon reservoirs*. London: Geological Society, pp. 141–155.

Martinez C, Truillet R. 1987. Evolution structurale et paléogéographique de la Tunisie. *Memoria de le Societa Italiana de Geologia* 38: 35–45.

Masse JP, Philip J. 1981. Cretaceous coral-rudistid buildups of France. In: Toomey DF, ed. *Fossil reef models*. European, Soc. Econ. Paleont. Mineral, Special 30: 399–426.

Melki S, Negra MH. 2004. The Abiod Formation in the Enfida area: Particular sedimentary features and reservoir properties and implications. In: *Tunisia Petroleum Exploration Conference, Tunisia, Entreprise Tunisienne d'Activités Pétrolières (ETAP)*, pp. 129–137.

Mielke P, Bär K, Sass I. 2017. Determining the relationship of thermal conductivity and compressional wave velocity of common rock types as a basis for reservoir characterization. *Journal of Applied Geophysics* 140: 135–144.

M'Rabet A, Mejri F, Burollet PF, Memmi L, Chandoul H. 1995. Catalog of types sections in Tunisia: Cretaceous. Entreprise Tunisienne d'Activités pétrolières (ETAP). Mem. 8A. Tunisia.

Nabawy BS. 2015. Impacts of the pore and petro-fabrics on porosity and lithology factor of Archie's equation for carbonate rocks. *Journal of African Earth Sciences* 108: 101–114.

Nabawy BS, Kassab MA. 2014. Porosity-reducing and porosity-enhancing diagenetic factors for some carbonate microfacies: A guide for petrophysical facies discrimination. *Arabian Journal Geosciences* 7(11): 4523–4539.

Nabawy BS, Géraud Y. 2016. Impacts of pore- and petro-fabrics, mineral composition and diagenetic history on the bulk thermal conductivity of sandstones. *Journal of African Earth Sciences* 115: 48–62.

Negra MH, Philip J. 1986. Stratigraphie et paléontologie des formations à rudistes et grands foraminifères du Campanien du Jebel Kébar (Tunisie centrale). *Géologie Méditerranéenne* 12: 49–57.

Negra MH, Gili E. 2004. The role of rudists formations in micrite production and stabilization. Example of the Upper Cretaceous rudist formations in Jebel el Kebar, Central Tunisia. *Courier Forschungsinstitut Senckenberg* 247: 193–205.

Negra MH, Jaballah J. 2021. The rudist-rich carbonate units in central Tunisia as markers of Late Cretaceous transgressive events. *Arabian Journal of Geosciences* 13: 1298.

Negra MH, M'Rabet A, Troudi H, El Asmi K, Saidi F. 1996. Lithofacies and paleogeographic evolution of the upper Cretaceous reservoir rocks in Central Tunisia. In: *Proceedings of the 5th Tunisian Petroleum Exploration Conference, Tunisia, Entreprise Tunisienne d'Activités Pétrolières (ETAP)*, pp. 173–190.

Njahi Z, Kassabi N, Touir J. 2017. Porosity and reservoir potentiality of the Cherahil Formation limestone (middle-upper Eocene) in the Gulf of Gabes (Tunisia). *Journal of African Earth Sciences* 131: 166–178.

Norton D, Knapp R. 1977. Transport phenomena in hydrothermal system: The nature of porosity. *American Journal of Science* 277: 913–917.

Nooruddin HA, Hossain ME, Al-Yousef H, Okasha T. 2014. Comparison of permeability models using mercury injection capillary pressure data on carbonate rock samples. *Journal of Petroleum Science and Engineering* 121: 9–22.

Pasquale V, Verdoya M, Chiozzi P. 2015. Measurements of rock thermal conductivity with a Transient Divided Bar. *Geothermics* 53: 183–189.

Philip J., 1985. Les formations à rudistes du Crétacé en Tunisie. *Une revue. Premier Congrès National des Sciences de la Terre, Tunis* 1: 235–240.

Philip J. 2003. Peri-Tethyan neritic carbonate areas: Distribution through time and driving factors. *Paleogeography, Paleoclimatology, Paleoecology* 196: 19–37.

Popov YA, Seminov VG, Korosteliov VM, Berezin VV. 1983. None-contact evaluation of thermal conductivity of rocks with the aid of a mobile heat source. *Physics of the solid Earth* 19: 563–567.

Popov YA, Berezin VV, Seminov VG, Korosteliov VM. 1985. Complex detailed investigation of the thermal properties of rocks based on a moving point source. *Physics of the solid Earth* 21: 64–70.

Popov YA, Pribnow DFC, Sass JH, Williams CF, Burkhardt H. 1999. Characterization of rock thermal conductivity by high resolution optical scanning. *Geothermics* 28: 253–276.

Popov Y, Tertychnyi V, Romushkevich R, Korobkov D, Pohl J. 2003. Interrelations between thermal conductivity ans other physical properties of rocks: experimental data. *Pure and Applied Geophysics* 160: 1137–1161.

Purser BH. 1975. Sédimentation et diagenèse précoce de séries carbonatées du Jurassique moyen de Bourgogne. Thèse de Doctorat, Université Paris-Orsay, 383 p.

Rashid F, Glover PWJ, Lorinczi P, Hussein D, Collier R, Lawrence J. 2015. Permeability prediction in tight carbonate rocks using capillary pressure measurements. *Marine and Petroleum Geology* 68: 536–550.

Rilem. 1978. Altération et protection des monuments en pierre, méthodes expérimentales conseillées. In: *Colloque international, Paris, 5–9 juin*.

Robaszynski F, Amédro F, Gonzalez-Donoso JM, Linares D. 2007. Les bio-évènements de la limite Albien (Vraconnien)-Cénomanien aux marges nord et sud de la Téthys (S.E. de la France et Tunisie centrale). *Carnets de Géologie. Notebooks on Geology* 2: 3–15.

Saïdi F, Ben Ismail MH, M'Rabet A. 1997. Les récifs Coniaciens à rudistes de Tunisie Centro-Occidentale : sédimentologie, cadre paléogéographique et interprétation séquentielle. *Journal of African Earth Sciences* 24(4): 531–548.

Salah MK, El Ghandour MM, Abdel-Hameed AMT. 2016. Effect of diagenesis on the petrophysical properties of the Miocene rocks at the Qattara depression, north Western Desert, Egypt. *Arabian Journal of Geosciences* 9(5): 329.

Salah MK, Alqudah M, David C. 2020. Acoustics and petrophysical investigations on upper cretaceous carbonate rocks from northern Lebanon. *Journal of African Earth Sciences* 172: 103955.

Salaj J. 1978. The geology of the Pelagian block: The eastern Tunisian Platform. In: Nairn AEM, Kanes WH, Stehli FG, eds. *The Ocean Basins and Margin: The western Mediterranean*. New York: Plenum Press 4(B), pp. 77–95.

Salmouna-Jomaa D. 2017. Lithostratigraphy and sedimentology of the Turonian-Coniacian Biréno-Douleb carbonates in Gafsa region: Correlation with the Gulf of Gabes. Thèse de Doctorat, Université de Tunis El Manar, Tunisia, 253 p.

Salmouna-Jomaa D, Chaabani F, Dhahri F, Mzoughi M, Salmouna A, Bessaies-Zijlstra H. 2014. Lithostratigraphic analysis of the Turonian-Coniacian Bireno and Douleb carbonate Members in Jebels Berda and Chemsi, Gafsa basin, central-southern Atlas of Tunisia. *Journal of African Earth Sciences* 100: 733–754.

Scheidegger AE. 1974. The physics of flow through porous media. University of Toronto Press, 353 p.

Scott RW. 2003. High resolution North African Cretaceous stratigraphy: Status. In: *North African Cretaceous Carbonate Plateform Systems*. Amsterdam: Kluwer Academic Publishers, pp. 1–17.

Skelton PW. 2003. In: Skelton PW, ed. The Cretaceous World. The Open University, Cambridge University Press, 360 p.

Skelton PW, Gili E. 1991. Palaeoecological classification of rudist morphotypes. In: *First International Conference on Rudists, Belgrade, Serbian Geological Society*, pp. 71–86.

Soete J, Kleipool LM, Claes H, Claes S, Hamaekers H, Kele S, *et al.* 2015. Acoustic properties in travertines and their relation to porosity and pore types. *Marine and Petroleum Geology* 59: 320–335.

Touati MA, Rodgers MR. 1998. Tectono-stratigraphic history of the southern gulf of Gabes and the hydrocarbon habitas. In: *Proceeding of the 6th Tunisian Petroleum Exploration And Production Conference, Tunisia, Entreprise Tunisienne d'Activités Pétrolières (ETAP)*, pp. 343–369.

Touir J, Soussi M, Troudi H. 2009. Polyphased dolomitization of a shoal-rimmed carbonate platform: example from the middle Turonian Bireno dolomites of central Tunisia. *Cretaceous Research* 30: 785–804.

Troudi H. 1998. Les réservoirs et faciès associés du Crétacé supérieur en Tunisie centrale : sédimentologie, stratigraphie séquentielle et diagenèse. Thèse de Doctorat, Université de Tunis, Tunisia, 287 p.

Troudi H, Negra MH, M'Rabet A. 1999. Predictive evaluation of Lower-Middle Turonian carbonate reservoir in Central Tunisia through integration of depositional environment and diagenesis. *Ann. Mines Géol.* 40: 81–98.

Vernik L. 1994. Predicting lithology and transport properties from acoustic velocities based on petrophysical classification of siliciclastic. *Geophysics* 59: 420–427.

Verwer K, Eberli GP, Weger RJ. 2011. effect of pore structures on electrical resistivity in carbonates. *American Association of Petroleum Geologists* 95(2): 175–190.

Wang Z, Nur A. 1992. Elastic wave velocity in porous media: A theorical recipe. In: Wang Z, Nur A, eds. *Seismic and acoustic velocities in reservoir rocks*. Geophysics, pp. 1–35.

Wardlaw NC, Taylor RP. 1976. Mercury capillary pressure curves and the interpretation of pore structure and capillary behavior in reservoir rocks. *Bulletin of Canadian Petroleum Geology* 24: 226–272.

Wardlaw NC, Cassan JP. 1978. Estimation of recovery efficiency by visual observation of pore systems in reservoir rocks. *Bulletin of Canadian Petroleum Geology* 26: 572–585.

Wardlaw NC, Mckellar M. 1981. Mercury porosimetry and interpretation of pore geometry in sedimentary rocks and artificial models. *Powder Technology* 29: 127–143.

Wardlaw NC, Yu L. 1988. Fluid topology, pore size and aspect ratio during imbibition. *Transport in Porous Media* 3: 17–34.

Washburn EW. 1921. Note on a method of determining the distribution of pores sizes in a porous material. *Proceeding of the National Academy of Science* 7: 115–116.

Watanabe N, Kusanagi H, Shimazu T, Yagi M. 2019. Local non-vuggy modeling and relations among porosity, permeability and preferential flow for vuggy carbonates. *Engineering Geology* 248: 197–206.

Wyllie MRJ, Gregory AR, Gargner GHF. 1958. An experimental investigation of factors affecting elastic wave velocities in porous media. *Geophysics* 23: 459–493.

Zagrarni MF. 1996. Sédimentologie, stratigraphie séquentielle et diagenèse des faciès du Crétacé supérieur du Jebel Biréno. Paléogéographies des plates-formes carbonatées du Cénomanien supérieur-Coniacien en Tunisie centrale. Thèse de Doctorat, Université de Tunis, Tunisia, 358 p.

Zagrarni MF, Negra MH, Melki S. 2003. Turonian rudist-coral limestones in Jebel Biréno, Central Tunisia. In: Gili E, Negra MH, Skelton P, eds. *North African Cretaceous Carbonate Platform Systems*. Amsterdam: Kluwer Academic Publishers, pp. 111–128.

Zagrarni MF, Negra MH, Melki S. 2008. The Cenomanian-Turonian Bahloul Formation in central-north Tunisia. Biosedimentary events and sequence stratigraphy. *Sedimentary Geology* 204: 18–35.

Zinszner B, Pellerin FM. 2007. A Geoscientist's guide to petrophysics. Publication de l'Institut Français du Pétrole, 384 p.

Zouari H, Turki MM, Deteil J, Stephan JP. 1999. Tectonique transtensive de la paléomarge tunisienne au cours de l'Aptien-Campanien. *Bulletin de la Société géologique de France* 3: 295–301.

Cite this article as: Boughalmi S, Géraud Y, Grosheny D, Ben Alaya S, Hedi Negra M. 2023. Characterization of proven Late Cretaceous Reservoir rocks in the Gulf of Gabes: Integrated case study, *BSGF - Earth Sciences Bulletin* 194: 8.